

Calhoun: The NPS Institutional Archive
DSpace Repository

Theses and Dissertations

1. Thesis and Dissertation Collection, all items

2017-03

Analysis of proton radiation effects on gallium nitride high electron mobility transistors

Augustine, Robert T.

Monterey, California: Naval Postgraduate School

<http://hdl.handle.net/10945/52977>

Downloaded from NPS Archive: Calhoun



Calhoun is a project of the Dudley Knox Library at NPS, furthering the precepts and goals of open government and government transparency. All information contained herein has been approved for release by the NPS Public Affairs Officer.

Dudley Knox Library / Naval Postgraduate School
411 Dyer Road / 1 University Circle
Monterey, California USA 93943

<http://www.nps.edu/library>



**NAVAL
POSTGRADUATE
SCHOOL**

MONTEREY, CALIFORNIA

THESIS

**ANALYSIS OF PROTON RADIATION EFFECTS ON
GALLIUM NITRIDE HIGH ELECTRON MOBILITY
TRANSISTORS**

by

Robert T. Augustine

March 2017

Thesis Advisor:

Todd Weatherford

Second Reader:

Matthew Porter

Approved for public release. Distribution is unlimited.

THIS PAGE INTENTIONALLY LEFT BLANK

REPORT DOCUMENTATION PAGE			Form Approved OMB No. 0704-0188	
Public reporting burden for this collection of information is estimated to average 1 hour per response, including the time for reviewing instruction, searching existing data sources, gathering and maintaining the data needed, and completing and reviewing the collection of information. Send comments regarding this burden estimate or any other aspect of this collection of information, including suggestions for reducing this burden to Washington headquarters Services, Directorate for Information Operations and Reports, 1215 Jefferson Davis Highway, Suite 1204, Arlington, VA 22202-4302, and to the Office of Management and Budget, Paperwork Reduction Project (0704-0188) Washington DC 20503.				
1. AGENCY USE ONLY (Leave Blank)	2. REPORT DATE MAR 2017	3. REPORT TYPE AND DATES COVERED Master's Thesis 05-30-2016 to 03-15-2017		
4. TITLE AND SUBTITLE ANALYSIS OF PROTON RADIATION EFFECTS ON GALLIUM NITRIDE HIGH ELECTRON MOBILITY TRANSISTORS			5. FUNDING NUMBERS	
6. AUTHOR(S) Robert T. Augustine				
7. PERFORMING ORGANIZATION NAME(S) AND ADDRESS(ES) Naval Postgraduate School Monterey, CA 93943			8. PERFORMING ORGANIZATION REPORT NUMBER	
9. SPONSORING / MONITORING AGENCY NAME(S) AND ADDRESS(ES) N/A			10. SPONSORING / MONITORING AGENCY REPORT NUMBER	
11. SUPPLEMENTARY NOTES The views expressed in this document are those of the author and do not reflect the official policy or position of the Department of Defense or the U.S. Government. IRB Protocol Number: N/A.				
12a. DISTRIBUTION / AVAILABILITY STATEMENT Approved for public release. Distribution is unlimited.			12b. DISTRIBUTION CODE	
13. ABSTRACT (maximum 200 words) In this work, a physics-based simulation of non-ionizing proton radiation damage effects at different energy levels on a GaN-on-silicon high electron mobility transistor was created. Based on physical results of 2.0-MeV protons irradiation to fluence levels of 6×10^{14} protons/cm ² , the simulation was tuned to match electron mobility μ_n and then compared to threshold voltage V_{th} on state resistance R_{on} and transconductance g_m . A Monte Carlo simulator was used to model two particle interactions utilizing the Kinchin and Pease model. The model was developed in Silvaco ATLAS, but the Athena and Victory Stress modules were also utilized. After comparison of changing characteristics between the model and the physical device at 2.0-MeV proton irradiation, predictions were made for 5.0, 10.0, 20.0 and 40.0-MeV proton irradiation. The model generally overpredicted damage in the lattice when compared to the physical results seen in prior work.				
14. SUBJECT TERMS gallium nitride, aluminum gallium nitride, high electron mobility transistor, electronics, 2 MeV proton irradiation, radiation effects			15. NUMBER OF PAGES 87	16. PRICE CODE
17. SECURITY CLASSIFICATION OF REPORT Unclassified	18. SECURITY CLASSIFICATION OF THIS PAGE Unclassified	19. SECURITY CLASSIFICATION OF ABSTRACT Unclassified	20. LIMITATION OF ABSTRACT UU	

NSN 7540-01-280-5500

Standard Form 298 (Rev. 2-89)
Prescribed by ANSI Std. Z39-18

THIS PAGE INTENTIONALLY LEFT BLANK

Approved for public release. Distribution is unlimited.

**ANALYSIS OF PROTON RADIATION EFFECTS ON GALLIUM NITRIDE HIGH
ELECTRON MOBILITY TRANSISTORS**

Robert T. Augustine
Lieutenant, United States Navy
B.S., United States Naval Academy, 2011

Submitted in partial fulfillment of the
requirements for the degree of

MASTER OF SCIENCE IN ELECTRICAL ENGINEERING

from the

**NAVAL POSTGRADUATE SCHOOL
March 2017**

Approved by: Todd Weatherford
Thesis Advisor

Matthew Porter
Second Reader

Clark Robertson
Chair, Department of Electrical Engineering

THIS PAGE INTENTIONALLY LEFT BLANK

ABSTRACT

In this work, a physics-based simulation of non-ionizing proton radiation damage effects at different energy levels on a GaN-on-silicon high electron mobility transistor was created. Based on physical results of 2.0-MeV protons irradiation to fluence levels of 6×10^{14} protons/cm², the simulation was tuned to match electron mobility μ_n and then compared to threshold voltage V_{th} on state resistance R_{on} and transconductance g_m . A Monte Carlo simulator was used to model two particle interactions utilizing the Kinchin and Pease model. The model was developed in Silvaco ATLAS, but the Athena and Victory Stress modules were also utilized. After comparison of changing characteristics between the model and the physical device at 2.0-MeV proton irradiation, predictions were made for 5.0, 10.0, 20.0 and 40.0-MeV proton irradiation. The model generally overpredicted damage in the lattice when compared to the physical results seen in prior work.

THIS PAGE INTENTIONALLY LEFT BLANK

Table of Contents

1	Introduction	1
1.1	Research Objective	2
1.2	Related Work	2
1.3	Thesis Organization	3
2	Background	5
2.1	Properties of Gallium Nitride	5
2.2	Spontaneous and Piezoelectric Polarization	6
2.3	Non-Ionizing Radiation Damage Effects	10
2.4	Non-Ionizing Radiation Damage in GaN	12
3	Model Development	15
3.1	Device Composition	15
3.2	Initial Device Characterization	16
3.3	SRIM Model	28
4	Model Implementation	33
4.1	Impurity Scattering Mobility Implementation	33
4.2	Model Evaluation Versus 2.0-MeV Experimental Results	34
4.3	Trap Occupancy and Modulation of the Electric Field	39
4.4	Model Evaluation at Additional Energy Levels.	44
5	Conclusions	47
	Appendix	49
A.1	SRIM Simulation Values	49
A.2	SILVACO Simulation Values.	52
A.3	Trap Levels in GaN	52

A.4 Code	53
Initial Distribution List	67

List of Figures

Figure 2.1	Crystal Structure. Source: [13].	5
Figure 2.2	Band Diagram. Source: [14].	5
Figure 2.3	Electronic Structure of an Aluminum Gallium Nitride (AlGaN)-GaN Heterostructure. Adapted from [15].	8
Figure 2.4	Source and Drain Resistance Diagram	10
Figure 2.5	Depiction of Particle Collision in a Crystal Lattice	11
Figure 3.1	Representation of the GaN High-Electron Mobility Transistor Gate Stack Structure	15
Figure 3.2	Scanning Transmission Electron Microscopy Photograph of a Single High-Electron Mobility Transistor from Reticle. Adapted from [11].	16
Figure 3.3	Device Created In ATLAS versus Scanning Transmission Electron Microscopy Imaging of Device. Adapted from [11].	17
Figure 3.4	Silvaco Generated Band Diagram Beneath the Gate Stack	18
Figure 3.5	V_g versus I_d $V_d = 100.0$ mV	20
Figure 3.6	V_g versus I_d $V_d = 10.0$ V	20
Figure 3.7	V_g versus I_d $V_d = 100.0$ mV	22
Figure 3.8	V_g versus I_d $V_d = 10.0$ V	23
Figure 3.9	Source and Drain Resistance Measurements	23
Figure 3.10	Athena Victory Stress Simulation	25
Figure 3.11	V_g versus I_d Comparison Between Model Output and Measured Results, $V_d = 100.0$ mV	26
Figure 3.12	V_g versus I_d Comparison Between Model Output and Measured Results, $V_d = 10.0$ V	27

Figure 3.13	I_d versus V_d Comparison Between Model Output and Measured Results, $V_g = -3.0, -2.0, -1.0$ and 0.0 V	27
Figure 3.14	Linear Fitting for 2.0-MeV Protons in GaN.	31
Figure 3.15	Linear Fitting for 2.0-MeV Protons in AlGaN	32
Figure 4.1	Percent Change in μ_{2deg} versus Fluence	34
Figure 4.2	Percent Change of Device Characteristics after 2 MeV Proton Irradiation.	35
Figure 4.3	Comparison Between Model Output and Experimental Results for Percent Change in V_{th} versus Fluence	36
Figure 4.4	Comparison Between Model Output and Experimental Results for Percent Change in R_{on} versus Fluence	36
Figure 4.5	Comparison Between Model Output and Experimental Results for Percent Change in $G_{m,sat}$ versus Fluence	37
Figure 4.6	V_g versus I_d Comparison, $V_d = 100.0$ mV	38
Figure 4.7	V_g versus I_d Comparison, $V_d = 10.0$ V	38
Figure 4.8	I_d versus V_d Comparison, $V_g = -3.0, -2.0, -1.0$ and 0.0 V	39
Figure 4.9	Trap and Donor Occupancy Levels (cm^{-3}) in the AlGaN Barrier Layer at Fluence level of 10^{11}cm^{-2}	40
Figure 4.10	Trap and Donor Occupancy Levels (cm^{-3}) in the AlGaN Barrier Layer at Fluence level of $6.0 \times 10^{14}\text{cm}^{-2}$	40
Figure 4.11	Trap and Donor Occupancy Levels (cm^{-3}) in the GaN Barrier Layer at Fluence level of 10^{11}cm^{-2}	41
Figure 4.12	Trap and Donor Occupancy Levels (cm^{-3}) in the GaN Barrier Layer at Fluence level of $6.0 \times 10^{14}\text{cm}^{-2}$	41
Figure 4.13	Electric Field Distribution at a Fluence of 10^{11}cm^{-2}	42
Figure 4.14	Electric Field Distribution at a Fluence of $6.0 \times 10^{14}\text{cm}^{-2}$	43

Figure 4.15	Electric Field Distribution at Fluences of 10^{11} cm^{-2} and $6.0 \times 10^{14} \text{ cm}^{-2}$	43
Figure 4.16	Percent Change in μ_{2deg} versus Fluence for Varying Proton Energies	44
Figure 4.17	Percent Change in V_{th} versus Fluence for Varying Proton Energies	45
Figure 4.18	Percent Change in R_{on} versus Fluence for Varying Proton Energies	45
Figure 4.19	Percent Change in $g_{m,sat}$ versus Fluence for Varying Proton Energies	46

THIS PAGE INTENTIONALLY LEFT BLANK

List of Tables

Table 3.1	Thermal Heating Coefficients	19
Table 3.2	Constant Values for GaN Regions	25
Table 3.3	Device Dimensions Listed from Top to Bottom	28
Table 3.4	TRIM Compound Setup Values	29
Table 3.5	TRIM Atomic Setup Values	29
Table 3.6	Interstitial and Vacancy Distribution Fitting Functions in the GaN Region of the Device	31
Table 3.7	Interstitial and Vacancy Distribution Fitting Functions in the AlGaN Region of the Device	32
Table A.1	Interstitial and Vacancy Fitting Functions in the GaN Region of the Device	49
Table A.2	Interstitial and Vacancy Fitting Functions in the AlGaN Region of Device	49
Table A.3	Interstitial and Vacancy Fitting Functions in the GaN Region of the Device	50
Table A.4	Interstitial and Vacancy Fitting Functions in the AlGaN Region of Device	50
Table A.5	Interstitial and Vacancy Fitting Functions in the GaN Region of the Device	50
Table A.6	Interstitial and Vacancy Fitting Functions in the AlGaN Region of Device	51
Table A.7	Interstitial and Vacancy Fitting Functions in the GaN Region of the Device	51
Table A.8	Interstitial and Vacancy Fitting Functions in the AlGaN Region of Device	51

Table A.9	Albrect Model Values. Adapted from [33]	52
Table A.10	Defects Introduced by Various Types of Irradiation in GaN. Adapted from [20].	52
Table A.11	Stated Energy Levels for Defects in GaN. Adapted from [20].	53

List of Acronyms and Abbreviations

2DEG	two-dimensional electron gas
III-N	III-Nitride
AlGaN	Aluminum Gallium Nitride
DoD	Department of Defense
GaN	Gallium Nitride
GaN-on-Si	GaN-on-silicon
HEMT	high-electron mobility transistor
K-P	Kinchin and Pease
NPS	Naval Postgraduate School
NRL	U.S. Naval Research Laboratory
PCF	polarized coulomb field
PKA	primary knock-on atom
RF	radio-frequency
SRIM	stopping and range of ions in matter
TCAD	technology computer-aided design

THIS PAGE INTENTIONALLY LEFT BLANK

Acknowledgments

I have no better way to say it than simply, thank you.

Thank you, Professor Weatherford.

Thank you, Matt Porter, for spending days of your life helping me.

THIS PAGE INTENTIONALLY LEFT BLANK

CHAPTER 1:

Introduction

The family of III-Nitride (III-N) semiconductor materials is used extensively in electronic devices requiring high-power density, high-temperature and high-frequency operation. Due to the wide band-gap and high mobility of III-N materials, devices fabricated using III-N materials outperform devices fabricated from related III-V semiconductors in breakdown voltage, radio-frequency (RF) power gain and thermal performance. The ability to fabricate III-N heterojunctions which lead to the formation of a high mobility, high density two-dimensional electron gas (2DEG) allow for the fabrication of high power RF transistors for use in applications where vacuum tubes have traditionally been the only option. Additionally, due to the high atomic threshold displacement energy of III-Ns, these materials promise superior reliability in environments where radiation effects are a concern.

The 2DEG formed in III-N heterostructures can be leveraged to create a three-terminal field-effect transistor, known as a high-electron mobility transistor (HEMT), which is optimally suited for RF applications. III-N HEMTs, particularly those fabricated using (0001) oriented Gallium Nitride (GaN)-Aluminum Gallium Nitride (AlGaN) heterostructures, are currently found in many of our next generation weapons and radar systems. High bandwidth shipboard communications, phased-array radar and electronic warfare modules are examples of systems that are already taking advantage of the properties wide band-gap III-Ns provide [1]–[3]. Due to the increased power density seen in GaN HEMTs, they are effective replacements for klystrons, which take significantly more space in shipboard applications. Another application for this technology is satellites. Again, because of their decreased size, modules leveraging GaN HEMTs save payload space without sacrificing capability. This is crucial for payload launch cost in space systems. The effects of radiation upon electronics in the space environment has been well documented over the years and provides engineers with different challenges as compared with terrestrial environments. Knowing how radiation affects device characteristics and reliability is of prime importance to the design of devices that will be used in space-based applications. Extensive research upon the effects of radiation upon the III-N material family has been carried out, but the understanding of the effects in devices, especially in GaN HEMTs, is not complete.

1.1 Research Objective

The effects of non-ionizing damage induced by high dose massive particle radiation on GaN-on-silicon (GaN-on-Si) HEMTs are explored using a physics-based technology computer-aided design (TCAD) model. The model is based upon GaN-on-Si HEMTs fabricated at the U.S. Naval Research Laboratory (NRL) for radiation experimentation. The Silvaco ATLAS TCAD package is used to first simulate the transport of charge carriers through the initial GaN-on-Si HEMT structure based upon measurements taken at the Naval Postgraduate School (NPS). Special attention is paid to accurate modeling of the mobility of the 2DEG channel, which is degraded by the presence of radiation damage.

Utilizing the stopping and range of ions in matter (SRIM) software package, we used a Monte Carlo simulator of heavy ion radiation damage within materials to generate damage profiles for interstitials and vacancies induced by proton irradiation of varying energies for the HEMT structure. The SRIM program utilizes the Kinchin and Pease (K-P) model of Frenkel pair generation to simulate damage events under heavy ion irradiation. Profiles were created for proton energies of 2.0, 5.0, 10.0, 20.0 and 40.0-MeV protons. These profiles were then inserted into the ATLAS model developed for the initial device. A literature review was conducted to identify and classify the energy levels of the related traps associated with vacancies and interstitials created by the radiation damage predicted by SRIM. Again, care was taken to select a physically realistic model of the mobility term which is affected by the presence of radiation induced defects.

Results were compared with data taken from prior work at NPS and NRL involving 2.0-MeV proton irradiation of the NRL devices to the model outputs. After modeling the effects of 2.0-MeV proton irradiation, we expanded the model to predict damage characteristics at the additional proton energy levels, with emphasis on predicting the expected change from 40.0-MeV proton irradiation for fluence levels above $10^{15} \text{ p}^+ \cdot \text{cm}^{-2}$.

1.2 Related Work

Studies conducted on proton radiation in AlGaIn/GaN HEMTs often have a wide variety of design variation between the devices. The manufacturing process, materials used and dimensions of the device all play a large role in the characteristics of the device. While it is impossible to find independent research with the identical devices utilized, Hu *et al.* have

done similar studies on 1.8-MeV proton irradiation of AlGaN/GaN-on-sapphire devices that are applicable to the study of the effects of proton radiation damage at similar and increased energy levels [4]–[6]. Modeling of radiation effects has also been studied. Hui-Chia Yu wrote an extensive paper on concepts of modeling diffusion of diluted species to varying complexities [7], [8].

At NPS, research on the radiation hardness of AlGaN/GaN HEMTs has been ongoing since the early 2000s. Initial research was carried out on commercial off-the-shelf devices. Thesis work at NPS started with properties research and failure analysis before moving to irradiation effects around six years ago [9]. More recently, research has been focused on the physical inspection of radiation damage in NRL fabricated GaN-on-Si HEMTs and the irradiation of these devices. In conjunction with NRL, work was carried out to irradiate and characterize GaN-on-Si devices using 2.0-MeV protons. Wade examined the micro-structure of damage created due to the irradiation by 2.0-MeV protons at a fluence of 6.0×10^{14} protons/cm² [10]. In that study, upon physical inspection of imagery provided by scanning transmission electron microscopy, voiding was noticed under the gate fingers of the device. This voiding was not originally present in the device. Along with this observation, energy dispersive spectroscopy analysis performed by Wessel revealed diffusion of Nickel into the Gold layer [11]. This diffusion at layer boundaries was also evident at the AlGaN/GaN interface. Fast neutron irradiation experimentation was also carried out. In an experiment by Iobst, NRL GaN-on-Si HEMTs were irradiated with gamma radiation to document the effects, followed by irradiation with fast neutrons (between 1.0 and 20.0 MeV) at the McClellan Nuclear Research Center. The effects of the gamma radiation were filtered from the effects of the fast neutron irradiation for analysis [12].

1.3 Thesis Organization

This thesis is laid out as follows. The device characterization, basic physics of proton interactions in a crystalline structure and principles of vacancy and interstitial creation and diffusion are reviewed in Chapter 2. The integration of physical properties into the Monte Carlo simulation software SRIM along with development of functions of damage related to depth based on simulation results are discussed in Chapter 3. The process for implementing these functions in the TCAD software Silvaco ATLAS along with the changes made to mobility modeling in order to more accurately encapsulate all of the effects contributing

to the changes in mobility exhibited in the device are also developed. In Chapter 4, the implementation of the radiation effects into the TCAD model is presented. The results of the model in comparison to physical results seen from 2.0-MeV proton radiation is analyzed, and predictions are made upon the damage induced by higher energy, higher fluence proton irradiation. Conclusions and opportunities for further work can be found in Chapter 5.

CHAPTER 2: Background

2.1 Properties of Gallium Nitride

Device quality III-N material has been available for device fabrication since the 1990s. For power and RF applications, the most important material in the III-N family is GaN. GaN is a wide band-gap semiconductor with a band-gap of approximately 3.4 eV at 300 K, dependent upon its crystal structure. The crystal structure of GaN can be either zincblende or wurtzite. The atomic structure and band diagram for wurtzite GaN are shown in Figures 2.1 and 2.2, respectfully. Wurtzite's crystal structure is hexagonal and is defined by two different lattice constants a and c . The wurtzite crystal structure is different from other crystal structures in that it lacks inversion symmetry. Due to this lack of inversion symmetry, GaN (and other III-Ns) are pyroelectric: they possess a net spontaneous polarization P_{sp} aligned antiparallel along the hexagonal c -axis of the crystal. Additionally, III-Ns are piezoelectric and modulate the polarization of the material dependent upon the strain in the lattice.

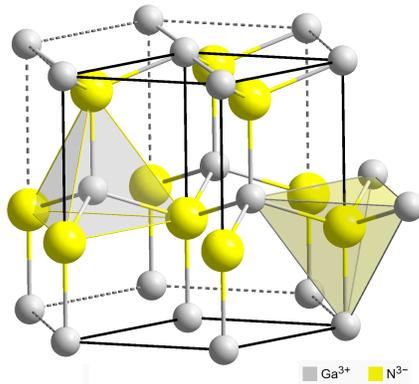


Figure 2.1. Crystal Structure. Source: [13].

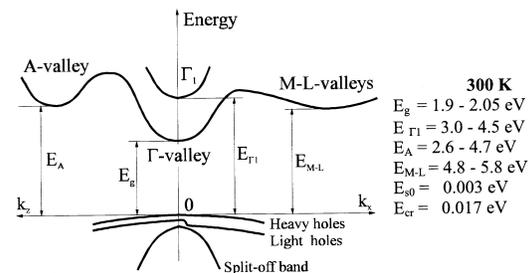


Figure 2.2. Band Diagram. Source: [14].

GaN is not an easy material to grow in bulk at reasonable cost, so it is often grown on a substrate. The use of a specific substrate can alter the material properties of the GaN. When creating devices, GaN is not grown directly on the substrates because differences in lattice constants result in strains that cause large defects in the GaN. This mismatch increases the dislocation density within the active region of the device, resulting in diminished device performance. For that reason, buffer layers are grown on the substrate before growing GaN. Each buffer layer absorbs a portion of the stress so that when GaN is deposited, the stress is at an optimal level for crystalline growth. Traditional substrates for III-N growth, such as sapphire and silicon carbide, can be expensive materials to manufacture and do not have the technological maturity of older materials such as Si. The desirability of Si as a substrate for growth stems from the ability to grow cheap, large, high quality substrates; however, the lattice mismatch between Si and III-Ns is severe. This necessitates the use of several additional buffer regions for successful III-N growth. In GaN-on-Si devices studied in prior research at NPS, aluminum nitride (AlN) in combination with varying mole fractions of AlGaN were used as transitional layers before the GaN layer.

The intrinsic strain developed in a crystal lattice is the result of an offset in the lattice constant between the growth layer and the substrate. This is referred to as lattice mismatch strain

$$\varepsilon = \frac{a_s - a_L}{a_L}, \quad (2.1)$$

defined by the lattice constants of the substrate a_s and the lattice constant of the layer making contact with it a_L . While too much strain can be a major issue during crystal growth, strain can be engineered to be useful in III-N structures. Once a high-quality III-N layer is grown, additional layers of III-Ns can be grown pseudomorphically, in which the entire epitaxial layer is under strain imposed via growth atop the substrate III-N layer. These additional layers create high quality heterojunctions which can be used for device applications.

2.2 Spontaneous and Piezoelectric Polarization

Polarization in III-Ns manifests as both spontaneous P_{sp} and piezoelectric P_{pz} polarization. The sum of these is the total polarization

$$P = P_{sp} + P_{pz}. \quad (2.2)$$

The units of polarization are C/cm². The spontaneous polarization can be calculated for III-N alloys by linearly interpolating between the known values of the two composite materials of the alloy. For example, for AlGaN of mole fraction x ,

$$P_{sp,AlGaN}(x) = P_{sp,AlN}x + P_{sp,GaN}(1 - x). \quad (2.3)$$

Piezoelectric polarization is defined as

$$P_{pz} = 2 \left(e_{13} - \frac{e_{33}c_{13}}{c_{33}} \right) \varepsilon, \quad (2.4)$$

where the value e_{ij} comes from the piezoelectric coupling matrix and has units of C/cm². The c_{ij} terms come from the stiffness matrix of the strained material and have units of GPa [15].

In real heterostructures, dislocations due to imperfect growth of the III-N substrate layer relax the strain in subsequent layers. This leads to a reduction in piezoelectric polarization. The degree of relaxation can be quantified by the unitless coefficient η , which varies between 0 and 1. The relaxation coefficient can be used to calculate the reduction in polarization in the heterostructure due to strain relaxation [15]

$$P_T = P_{sp} + (1 - \eta)P_{pz}. \quad (2.5)$$

The net effect of polarization is equivalent to the placement of a fixed sheet charge at the endpoints of the material layer. In a heterojunction, the net fixed charge is determined by the polarization difference between the two materials. This fixed charge is depicted in Figure 2.3(b). The sign of the charge at the interface depends upon the growth direction of the heterostructure. In an AlGaN/GaN heterostructure grown in the (0001) direction, this sheet charge is positive. In order to maintain net charge neutrality, electrons accumulate to screen out this sheet charge at the interface. This is called a 2DEG due to the fact that the large electric field in the GaN results in the electrons being quantum mechanically confined in a triangular quantum well. The energy band diagram of such a structure is shown in Figure 2.3, where the presence of the 2DEG can be clearly seen where the Fermi level goes above the conduction band in the GaN layer.

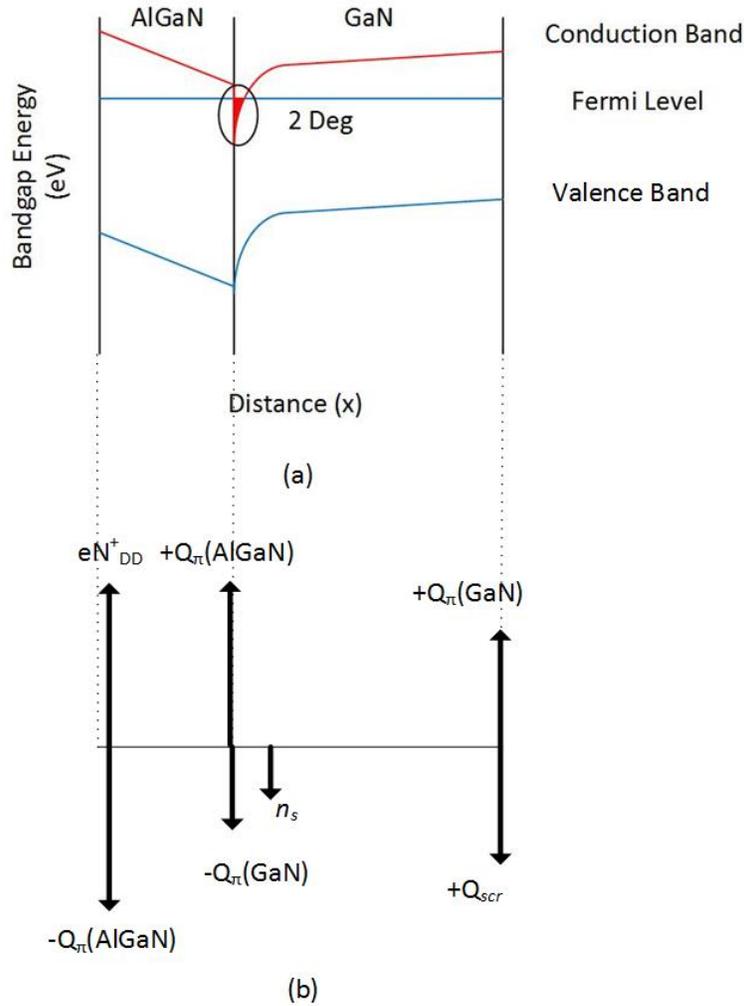


Figure 2.3. Electronic Structure of an AlGaN-GaN Heterostructure. Adapted from [15].

The band diagram and the sheet charge distribution of a representative AlGaN-GaN heterostructure are shown in Figures 2.3(a) and 2.3(b), respectively, where eN_{DD}^+ is the charge from surface defects at the top of the AlGaN layer, $-Q_{\pi}(\text{AlGaN})$ is the polarization of the AlGaN at the top of the layer, $+Q_{\pi}(\text{AlGaN})$ and $-Q_{\pi}(\text{GaN})$ are the polarizations at the AlGaN/GaN interface, $+Q_{\pi}(\text{GaN})$ is the polarization at the bottom of the GaN region, and $+Q_{scr}$ is the charge from defects at the GaN-substrate interface.

2.2.1 DC Characteristics of GaN HEMTs

A HEMT is a three-terminal device based upon the modulation of the conductivity of a 2DEG channel in a heterostructure. Such a device is easily fabricated through the deposition of a Schottky barrier upon the heterostructure and two ohmic contacts to contact the 2DEG. In an ungated heterostructure the 2DEG cannot be modulated directly. The Schottky gate contact is used to control the concentration of the 2DEG and can deplete the 2DEG given enough applied gate voltage.

The DC characteristics of a HEMT gatestack can be analyzed through energy and charge balance considerations. From such an analysis, the values for the gate threshold voltage [16]

$$V_{th} = \phi_b - \frac{-\Delta E_c}{q} - \frac{\Delta P}{C'_{eff}} \quad (2.6)$$

necessary to deplete the 2DEG channel can be calculated, where ϕ_b is the barrier height of the Schottky contact, ΔE_c is the conduction band energy level difference between the AlGaN and GaN layers, ΔP is the difference in polarization between the AlGaN and GaN layers, C'_{eff} is the capacitance due to the thickness of the AlGaN layer and the 2DEG offset due to quantum mechanical confinement of the 2DEG, and q is the electron charge. The equilibrium 2DEG concentration can be calculated from [16]

$$n_{2deg} = \frac{-V_{th}C'_{eff}}{q}. \quad (2.7)$$

The DC drain current for GaN HEMTs

$$I_D = \frac{W}{L} \mu C_{eff} \left((V'_{gs} - V_{th})V'_{ds} - \frac{V'^2_{ds}}{2} \right) \quad (2.8)$$

where W is the width of the device, L is the gate length, μ is the mobility, C_{eff} is the capacitance due to the thickness of the AlGaN layer and the 2DEG offset due to quantum mechanical confinement of the 2DEG, V'_{gs} , V'_{ds} and V'_{ds} are the voltages at the points shown in Figure 2.4, and V_{th} is the threshold voltage, which describes the drain current dependence upon the local voltages beneath the gate contact and does not take into account resistances that are present in the source and drain access region of the device.

Based on the diagram of the device shown in Figure 2.4, Equation 2.8 can be modified based on voltage loop calculations to include the effects of the access resistances.

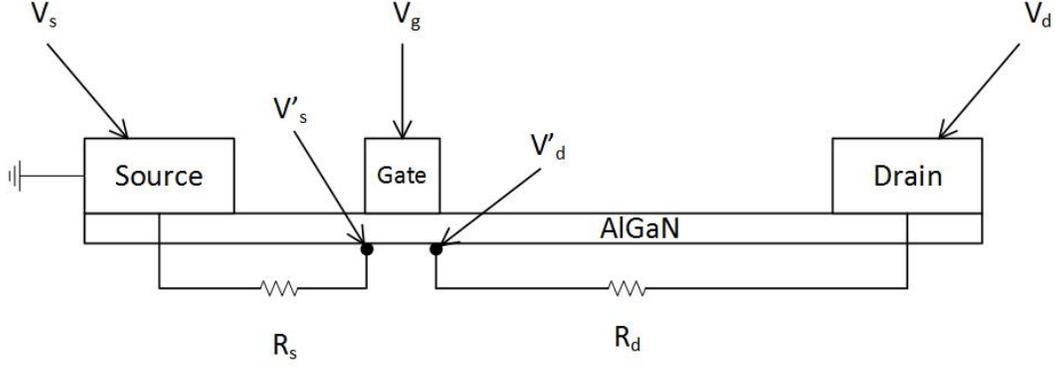


Figure 2.4. Source and Drain Resistance Diagram

The relationship between the applied drain and gate voltages V_{ds} and V_{gs} and the gate-edge referenced drain and gate voltages V'_{ds} and V'_{gs} are given by

$$V_{ds} = IR_s + IR_d + V'_{ds} \quad (2.9)$$

and

$$V_{gs} = IR_s + V'_{gs}. \quad (2.10)$$

From considerations of the 2DEG equilibrium concentration and electron mobility, the value of the resistances in the two access regions around the gate can be derived as [16]

$$R_d = \frac{L_{gd}}{Wq\mu_n n_{2deg}} \quad (2.11)$$

where L_{gd} is the distance between the gate edge and the drain edge. These parameters are important to the device and affect the characteristic curves of the device. The resistance values in these regions have a large effect on the device at higher drain currents.

2.3 Non-Ionizing Radiation Damage Effects

When an ionized particle moves through a crystal lattice, it interacts with the atoms in the lattice. These particles may directly collide with atomic nuclei physically or may "collide"

with atoms through charge interaction. The probability of a high energy ion colliding with atoms in the lattice is inversely proportional to the energy level of the ion [17]. When a collision does occur, conservation of energy and momentum is maintained and there can be a number of outcomes. If the particle has enough energy to overcome the energy required to displace the atom, known as the threshold displacement energy E_{th} , it knocks the lattice atom out of place. This creates an ionized atom that moves through the lattice with an energy dependent upon the nature of the collision, and a vacancy is left where it was before the collision. This atom is known as a primary knock-on atom (PKA). Depending on the amount of energy transferred to the PKA, we know it either comes to rest or continues to move. If it comes to rest, it either becomes an interstitial atom or replaces a vacancy in what is known as a replacement collision. If the atom continues to move, it may go on to collide with additional atoms. The atom continues to move and collide until its energy decreases below E_{th} , creating additional damage. Interstitial and vacancies remaining after the damage event are known as Frenkel pairs. A simple depiction of this process is seen in Figure 2.5.

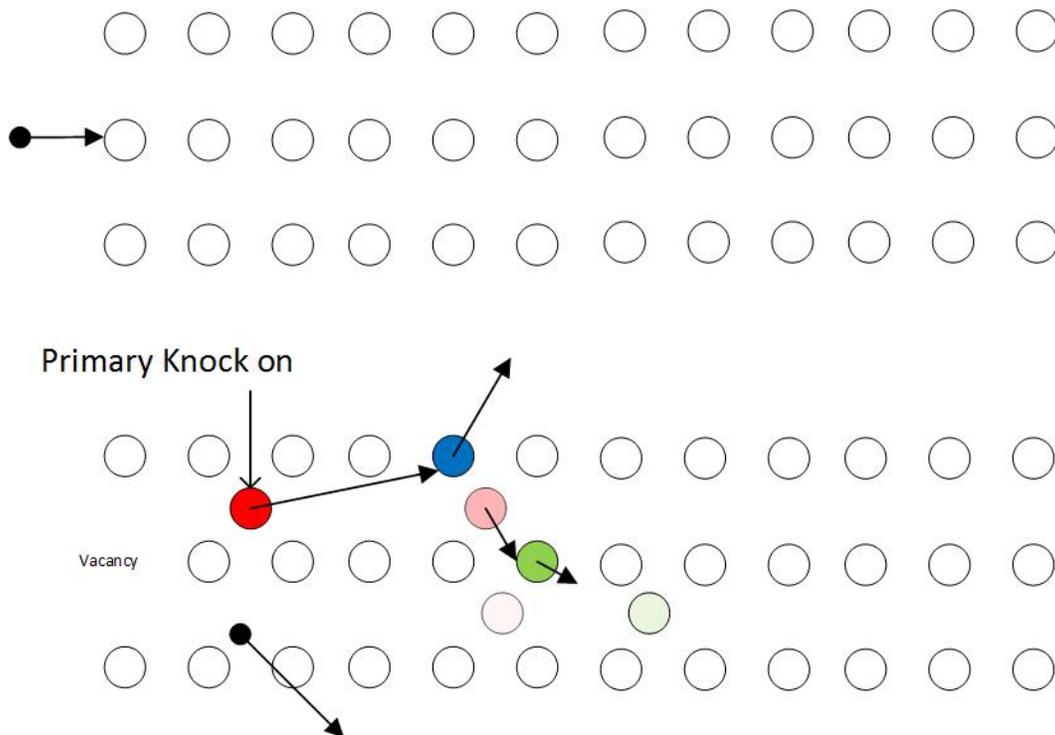


Figure 2.5. Depiction of Particle Collision in a Crystal Lattice

The radiation damage events are classified as two-particle scattering events, involving only the incident ion and the impacted lattice atom. In lower energy collisions, there may be more than two particles involved in a collision event. As the majority of non-ionizing radiation damage of concern in semiconductors is induced by high energy particles, this work only considers the effects of two-particle interactions.

2.4 Non-Ionizing Radiation Damage in GaN

Exposing the semiconductor materials to non-ionizing radiation damage causes several different effects. The first is damage to the lattice. When atoms are displaced from their ordered lattice locations to a more disordered location, electron trap states are created. There are several types of trap states. They can be either acceptor or donor traps. Both types can potentially accept or donate more than one electron or hole. If a trap state is filled, it is said to be ionized. If enough trap states are ionized in a region, this results in charge build up, which can alter the field levels within a device and lead to shifts in the device characteristics. This can lead to undesired changes in circuit operation.

In GaN layers, three trap states are known to be common after proton irradiation of fluence levels above 10^{12} protons/cm². These are referred to as ER1, ER2 and ER3. The "E" stands for electron traps, and the "R" indicates that it was developed from high-energy particle irradiation. Work by Auret in [18] has found that these three energy levels are found at 0.13, 0.16 and 0.2 eV below the conduction band of GaN after 2.0-MeV proton irradiation. Auret does not specifically attribute these defects to specific defect types or atoms, and they are all shallow traps. In other work by von Bardeleben, a nitrogen split interstitial defect is noted in GaN after 12.0-MeV proton irradiation to fluence levels of 8×10^{16} protons/cm² which occurs around 1.0 eV below the conduction band by using electron paramagnetic resonance [19]. Most notably, a review of radiation effects by Pearton [20] examined and attempted to fingerprint individual radiation induced defects in the GaN lattice and the trap energy levels associated with them. In general, radiation induces nitrogen vacancies which act as shallow donors at 0.06 eV below the conduction band, nitrogen interstitials acting as deep acceptors around 1.0 eV below the conduction band, Ga vacancies forming deep acceptors at 1.0 eV above the valence band, and Ga interstitials forming deep donors at 0.8 eV below the conduction band.

The crystal lattice is constantly vibrating and moving because of thermal energy maintained by the atoms and their bonds. This allows atoms in the lattice to change their position without any outside influence. If the temperature is not to the point of melting the material, the device can anneal out vacancies and interstitials. After irradiation events, devices try to return to their original form, and device characteristic have been seen to recover from these effects even at temperatures as low as 100 K [21]. In this work, He, Ar, O, Au, Te and Xe ions were implanted in GaN grown on sapphire at 15 K and Rutherford Backscattering analysis was performed to identify movement of ions as temperature was increased.

Sometimes, when radiation displaces an atom, the atom is transferred enough energy to move it substantially from its vacancy. This makes it difficult for it to return and anneal out of existence or return to ordered form. When larger amounts of damage are created, piles of interstitials and vacancies start to form, and irreversible voiding occurs in the material. This has been seen in work at NPS in [10] and work by Limpijumnong in [22]. In [10], Wade visually inspected a HEMT that had undergone 2.0-MeV proton irradiation and found an accumulation of vacancies manifesting as a void under the Ni gate finger of the device. Limpijumnong's work sought to classify and explain native defect diffusion in GaN crystal lattice through density functional theory.

THIS PAGE INTENTIONALLY LEFT BLANK

CHAPTER 3: Model Development

3.1 Device Composition

The GaN-on-Si wafers for the HEMT used in this study were grown by Nitronex Inc. The substrate is 350- μm thick Si. A silicon nitride (SiN_x) interface layer with a width of 2.0-nm and an AlN buffer layer of 300.0 nm were grown as an initial growth buffer layer, followed by two layers of AlGaN. The first is 400.0-nm thick with an Al mole fraction of 0.7, while the second is 300.0 nm thick with an Al mole fraction 0.4. A 0.8 μm high quality GaN layer was grown on top of the compliance layer. A 17.5-nm thick AlGaN layer with an Al mole fraction of 0.27 was grown pseudomorphically as a barrier layer to form the 2DEG channel. HEMT Device fabrication was carried out at NRL. The device gatestack consists of a 30.0-nm thick Ni gate, followed by a gold overlay of 300.0-nm. The device is passivated with a 100.0-nm thick SiN_x layer. Ohmic contacts to the 2DEG were formed via the deposition of a Ti/Al/Ni/Au alloy followed by rapid thermal annealing. The diagram of the HEMT gate stack structure is shown in Figure 3.1.

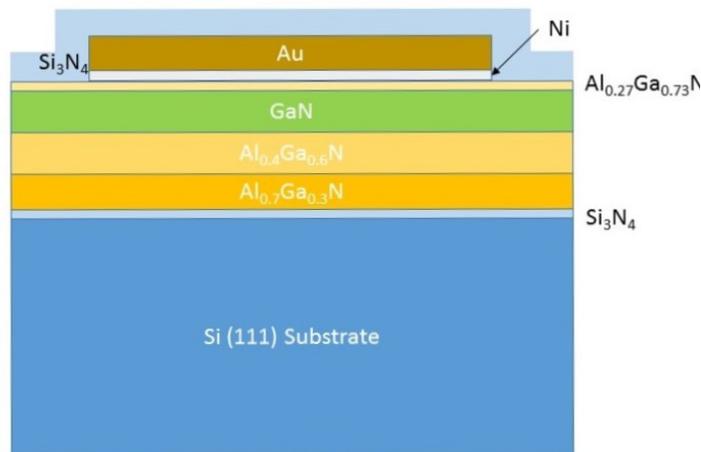


Figure 3.1. Representation of the GaN High-Electron Mobility Transistor Gate Stack Structure

3.2 Initial Device Characterization

The initial device electrical characterization was carried out using a probe station and a Keysight B1500A semiconductor parameter analyzer. DC IV measurements were performed to characterize the I_{ds} versus V_{gs} transfer characteristics, I_{gs} versus V_{gs} gate leakage, and I_{ds} versus V_{ds} characteristics of the device. Thirty-six devices on three identical reticles were tested to identify a device that could serve as a baseline for the development of the non-irradiated portion of the model. The section of the reticles considered had geometries identical to those used in 2.0-MeV irradiation experiments performed upon these devices in past work. The device dimension of the selected device are illustrated in Figure 3.2 in units of μm .

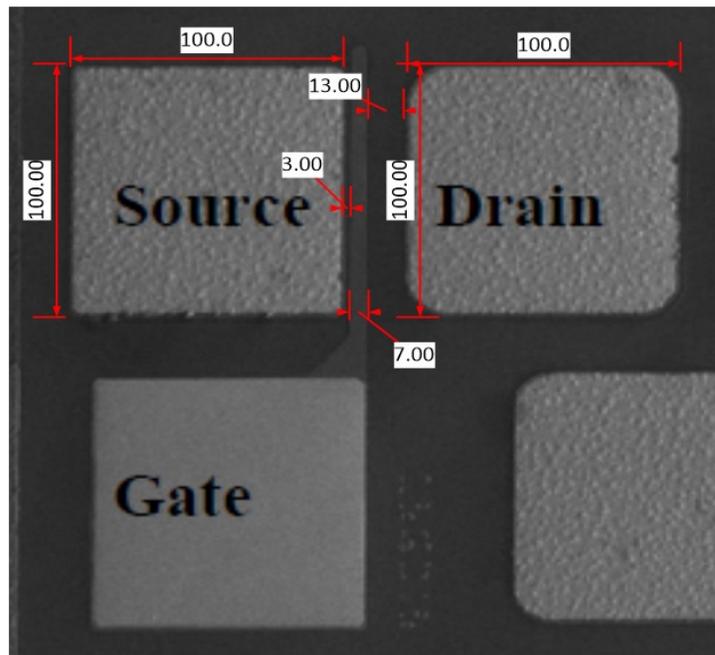


Figure 3.2. Scanning Transmission Electron Microscopy Photograph of a Single High-Electron Mobility Transistor from Reticle. Adapted from [11].

3.2.1 Initial Silvaco Model Development

The initial model of the device was created in Silvaco ATLAS based on the physical dimensions of the actual device as seen in Figure 3.3.

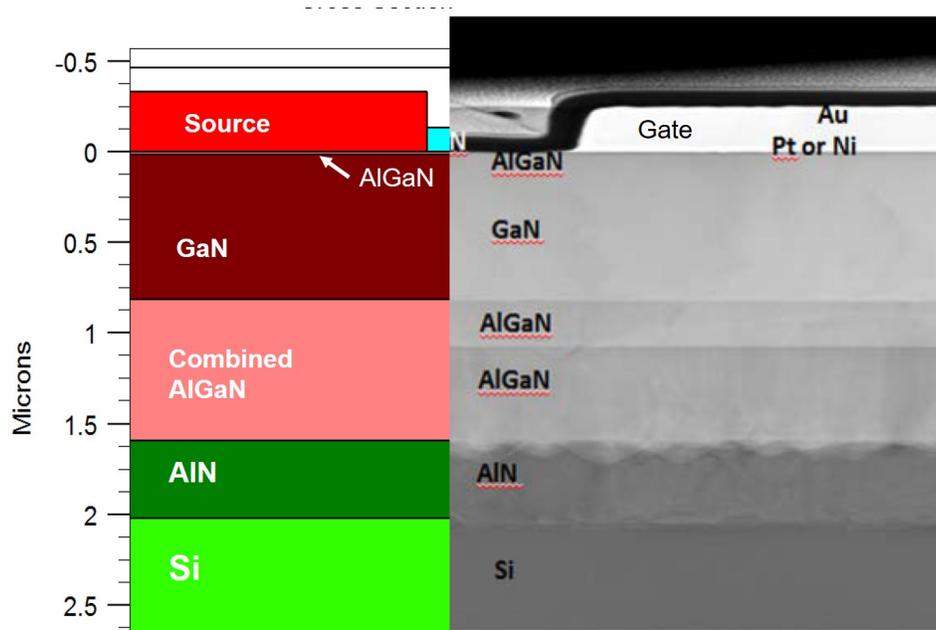


Figure 3.3. Device Created In ATLAS versus Scanning Transmission Electron Microscopy Imaging of Device. Adapted from [11].

The mesh was emphasized around the GaN and AlGaIn interface and vertically under the edges of gate. Initially, a built-in polarization statement, `polarization`, was used for the AlGaIn and GaN layers to simulate the spontaneous and piezoelectric polarization. Neither the AlN nor the AlGaIn buffer layers received polarization statements because of the defective nature of these layers in the device. These layers are assumed not to provide any net polarization. Using these basic model parameters, we extracted the band diagram seen in Figure 3.4, showing the presence of a 2DEG at equilibrium.

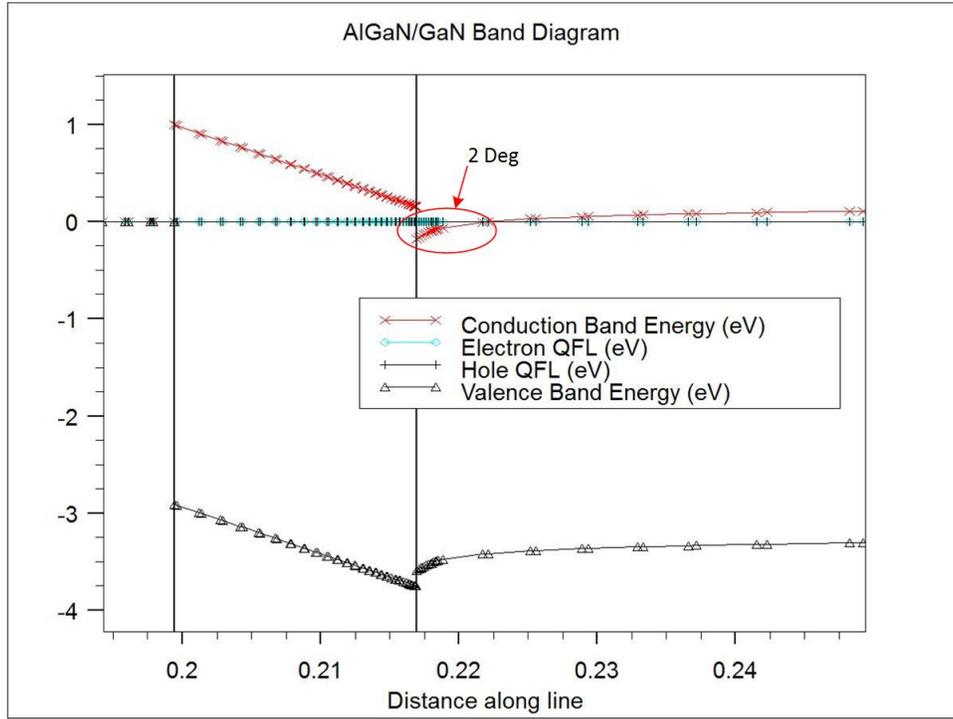


Figure 3.4. Silvaco Generated Band Diagram Beneath the Gate Stack

The polarization statement was replaced with a sheet charge statement in the final version of the model. This provides the same effect and does not alter the models characteristics. The relaxation coefficient η , defined in Equation 2.5, was adjusted to calculate the appropriate sheet charge to fit 2DEG density measured via Hall measurements [23]. In order to model heating throughout the device, a temperature dependent thermal conductivity model was utilized, implemented via `TCON.POWER` from ATLAS' GIGA self-heating module, for each material in the device. The characteristic equation for the thermal conductivity model is

$$k(T) = \frac{\alpha}{(T_L/300)^\beta}. \quad (3.1)$$

The units for k are W/cmK and the coefficients α and β for their respective layers are found in Table 3.1.

Table 3.1. Thermal Heating Coefficients

Material	α	β
$Al_{0.27}Ga_{0.73}N$	1.381	0.317
GaN	0.65	0.28
$Al_{0.3}Ga_{0.7}N$	0.688	1.5535
AlN	1.425	1.64
Si	1.48	0
Au	2.0	0
Ni	1.58	0

The source, drain, and gate were added to the simulation with electrode statements. The source and drain were modeled as ohmic contacts with work functions of 3.6 eV to match the affinity of the AlGa_{0.73}N and with an intrinsic 10.0-Ω resistance. The 10.0-Ω resistance was added to appropriately simulate the measured contact resistance of the ohmic contacts. The gate was modeled as a Schottky contact with a barrier height of 1.1 eV. The Shockley Reed Hall model was used to simulate carrier recombination in the model.

3.2.2 Mobility Modeling

Using appropriate mobility models is a key aspect in accurately modeling III-N devices. An initial, static value of 1260 cm²/(V · s) was adopted from Hall measurements taken on the bare reticle [23]. We quickly noted that, based on measured I-V characteristics, this value resulted in a large overestimate of device currents. Comparison between measured device characteristics and the results of this initial mobility model are shown in Figures 3.5 and 3.6.

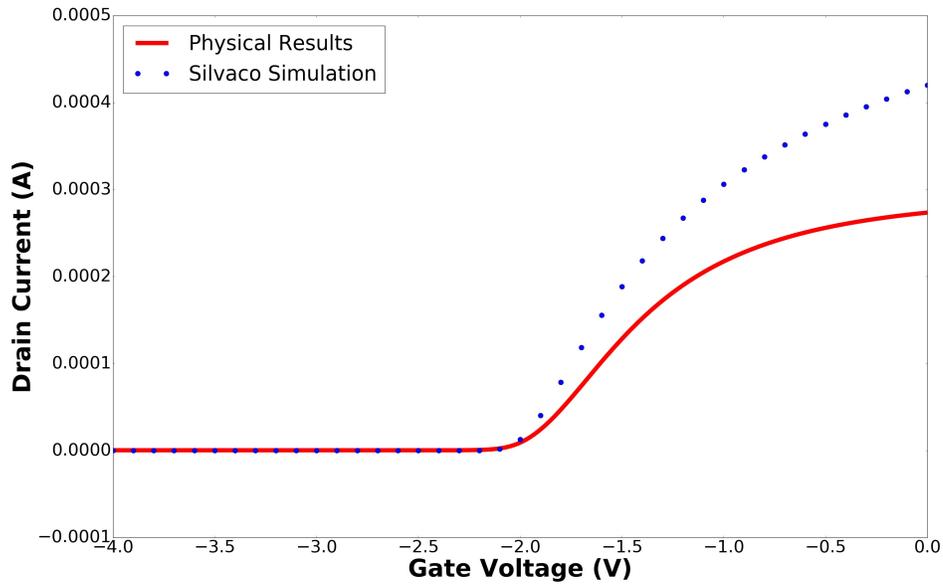


Figure 3.5. V_g versus I_d $V_d = 100.0$ mV

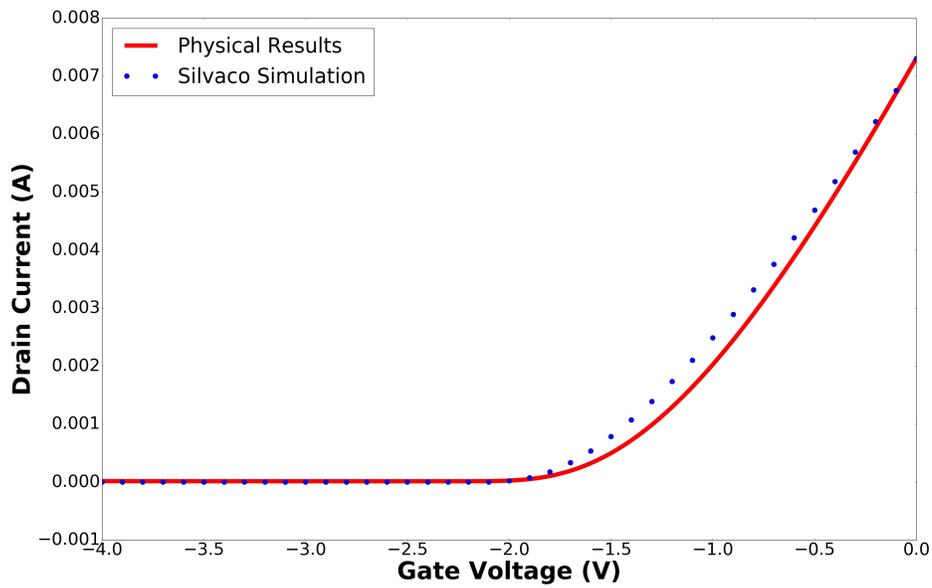


Figure 3.6. V_g versus I_d $V_d = 10.0$ V

Initial attempts at accurate mobility modeling were undertaken by implementing a custom mobility model within the GaN layer of the device. ATLAS allows users to create a custom mobility model which can be implemented via a c-function through the `tofimum` flag in the `mobility` statement. As a starting point, the well-known Albrecht model

$$\frac{1}{\mu(N, T_L)} = \frac{A \cdot N}{N_0} \left(\frac{T_L}{T_0} \right)^{\frac{-3}{2}} \ln \left[1 + 3 \left(\frac{T_L}{T_0} \right)^2 \left(\frac{N}{N_0} \right)^{\frac{-2}{3}} \right] + B \times \left(\frac{T_L}{T_0} \right)^{\frac{3}{2}} + \frac{C}{\exp\left(\frac{T_1}{T_L}\right) - 1}, \quad (3.2)$$

was utilized for GaN low-field mobility [24]. In the Albrecht model, $\mu(N, T_L)$ is the mobility as a function of doping and lattice temperature, N is the total doping concentration in cm^{-3} , N_0 is the initial doping concentration in cm^{-3} and T_L is the lattice temperature in K. Parameters A, B and C are scaling factors to adjust the impact of the individual terms of Equation 3.2. It is important to note that Equation 3.2 was developed for bulk GaN. Because the Albrecht model was derived for bulk material, it is technically incorrect to use it to model electron mobility in the 2DEG. The first term of the model,

$$\frac{A \cdot N}{N_0} \left(\frac{T_L}{T_0} \right)^{\frac{-3}{2}} \ln \left[1 + 3 \left(\frac{T_L}{T_0} \right)^2 \left(\frac{N}{N_0} \right)^{\frac{-2}{3}} \right], \quad (3.3)$$

accurately models impurity scattering in the bulk but not in the 2DEG. The second and third term, used to model acoustic and polar optical phonon scattering, can be shown to have the same temperature dependence as the corresponding mobility terms in the 2DEG-specific model [25]; therefore, those terms were incorporated as is and provided the foundation for the model. Charge dislocation and alloy scattering are additional factors that this model does not individually tailor terms for but can be shown as well to be constants independent of temperature and, thus, are incorporated in the tuning of the Albrecht model's B and C terms. The values for the B and C coefficients were initially scaled to give an initial mobility matching that of the measurements in [26].

For high field mobility, the Barnes model was utilized [27]. The Barnes model is

$$\mu_E = \frac{\mu_{n0} + (V_{sat}/E) (E/E_{crit})^\gamma}{1 + (E/E_{crit})^\gamma}, \quad (3.4)$$

where μ_{n0} is the low field mobility, V_{sat} is the saturation velocity, E is the electrical field, E_{crit} is the critical electrical field value, and γ is a unit less exponential fitting term. The Barnes model derives from measurements of the 2DEG electron velocity field scattering [27]. Values used for V_{sat} and E_{crit} were 3.0×10^7 and 20.0×10^3 , respectively. Based on recent work, other high field models showing velocity overshoot under conditions of high electric field may not be accurate [28]. In the work by Bajaj, high fields were utilized to try to reach velocity overshoot but found that electron velocity did not overshoot but merely saturated. More importantly, mobility overshoot was found to occur. This model also exhibits mobility overshoot, which fits the physical characteristics more accurately.

Although modulation of the Albrecht scale factors brought the simulated output currents into line with measured values, significant difficulty was found matching simulated to measured IV characteristics in regions of bias where the current was limited by access resistances as seen in Figures 3.7 and 3.8. To mediate this difficulty, measurements were taken to determine the access resistance for the gate and source regions of the device and can be seen in Figure 3.9.

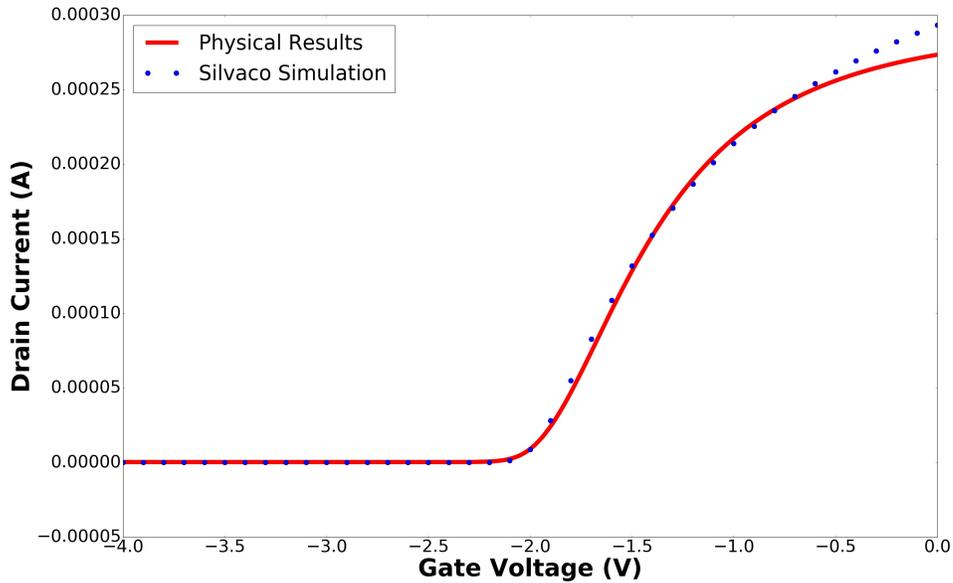


Figure 3.7. V_g versus I_d $V_d = 100.0$ mV

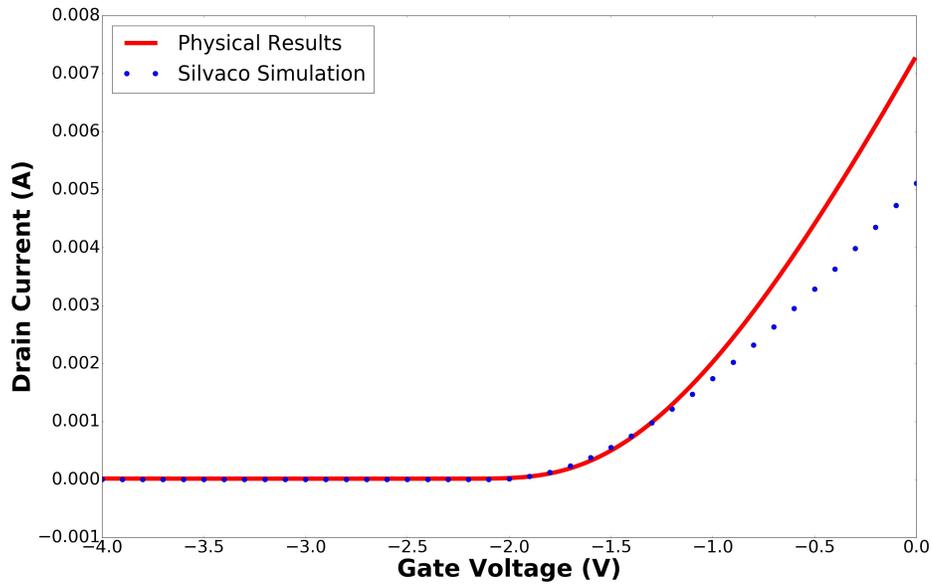


Figure 3.8. V_g versus I_d $V_d = 10.0$ V

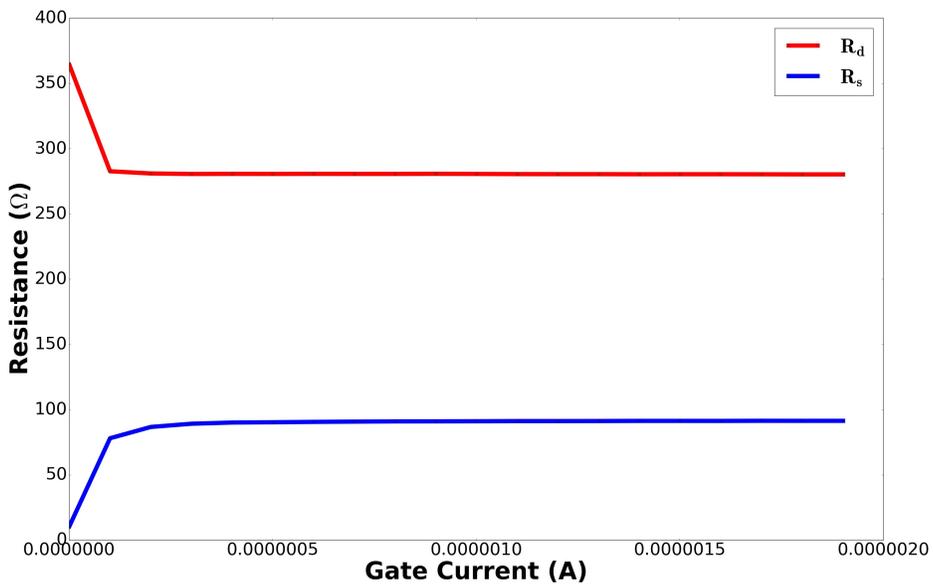


Figure 3.9. Source and Drain Resistance Measurements

From Equation 2.11, the width in the source and drain regions along with the n_{2deg} values should be the constant in a device. This leaves the mobility term and the length of the region that differs between the source and drain. If the ratio of the resistances is not equal to the ratio of the access region lengths, then the mobility term must be the source of variation. The ratio of resistances in this device is 280/90, which is not equal to the ratio of the access region lengths, 13/2.

From this information, an additional factor which could explain the measured deviation of access region mobility from expected values was sought. Recent work by Lin to explain the discrepancy in [29], [30], proposed that the mobility in the access regions is reduced due to an effect known as polarized coulomb field (PCF) scattering. PCF scattering is due to the fact that strain in the AlGa_N-Ga_N interface region is not constant throughout the device. The strain is changed by the deposition of materials such as the source, gate and drain metal and the passivation layer. This alters the electron mobility as a function of distance between the source and drain of the device. As a result, the mobility model was expanded to include this effect. In order to properly account for PCF scattering potentially induced by deposition of additional layers above the AlGa_N, the Silvaco model was shifted from ATLAS to Athena in order to utilize Silvaco's Victory Stress functionality. After running the model in Victory Stress, non-uniform strain under the nitride layer was apparent as seen in Figure 3.10 which shows the XX component of strain in the lattice. The variation of the strain causes scattering and a decrease in electron mobility from the measured values predicted by Hall measurements on a bare heterojunction.

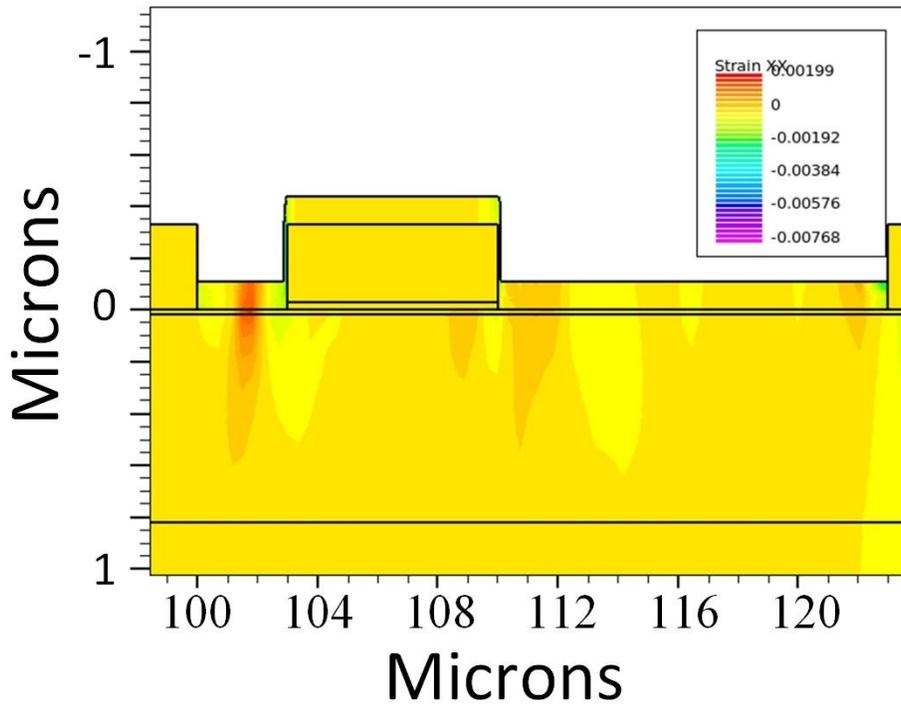


Figure 3.10. Athena Victory Stress Simulation

Although Victory Stress could not be used to directly predict the effects of inhomogeneous strain in the AlGaIn layer upon the mobility, the effects of PCF scattering were implemented in another way. In order to take into account the PCF scattering, the GaN region of the device was split into three sections. This allowed us to construct slightly different mobility terms for each region based on the resistances derived for each region. The resulting constants used to fit the mobility are presented in Table 3.2

Table 3.2. Constant Values for GaN Regions

	GaN Region 0	GaN Region 1	GaN Region 2
A	0.25	0.25	0.25
B	4.0	1.35	2.0
C	4.0	1.35	2.0

3.2.3 Final Model Evaluation

Our initial comparison between the physical device and the simulated device did not include any radiation effects and was used as a measure for the accuracy of our starting model. After scaling the model, a strong correlation to the physical device is shown in the characteristic IV curves illustrated in Figures 3.11, 3.12 and 3.13.

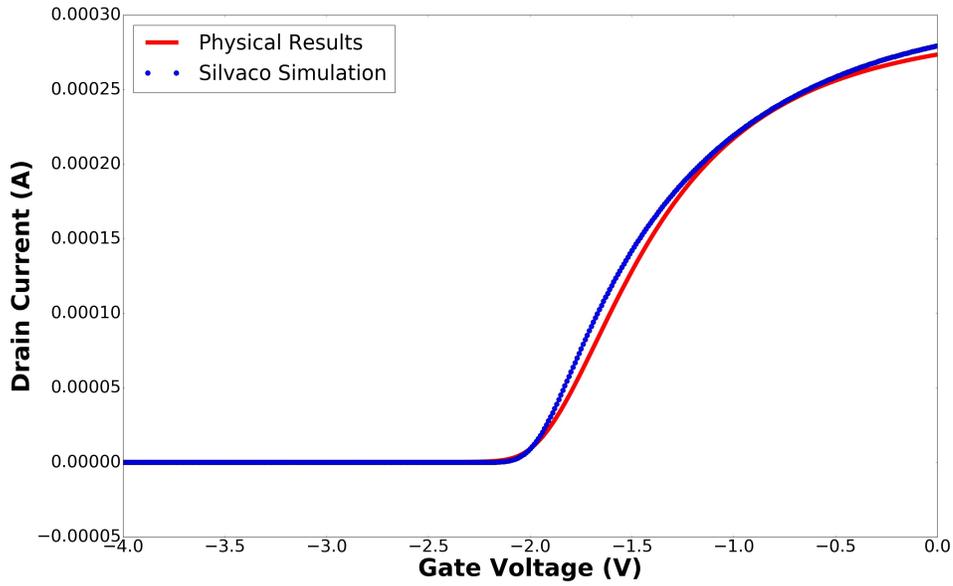


Figure 3.11. V_g versus I_d Comparison Between Model Output and Measured Results, $V_d = 100.0$ mV

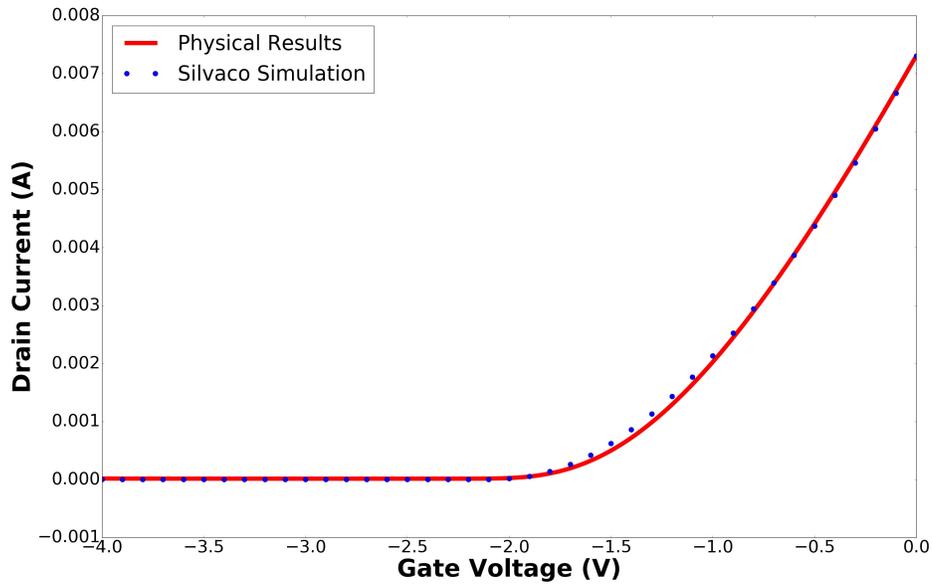


Figure 3.12. V_g versus I_d Comparison Between Model Output and Measured Results, $V_d = 10.0$ V

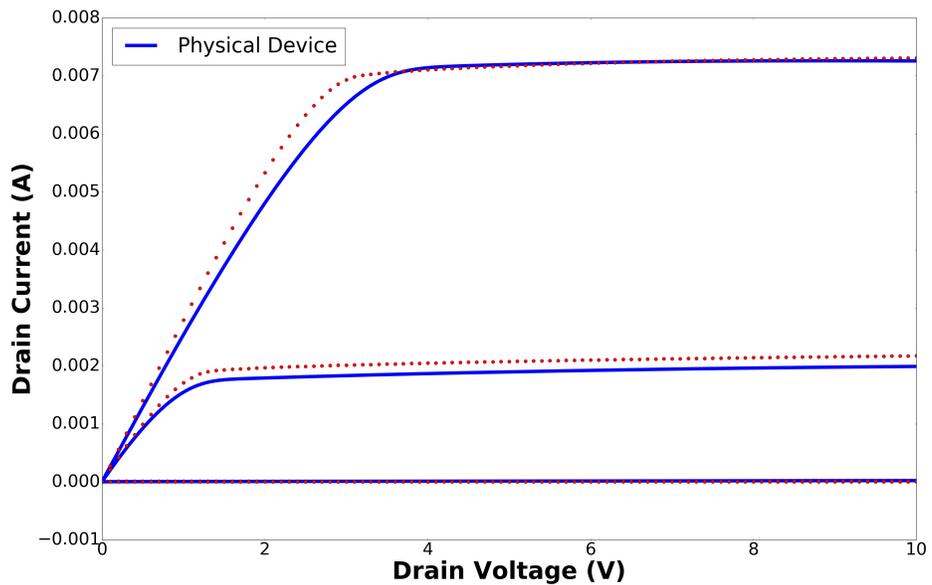


Figure 3.13. I_d versus V_d Comparison Between Model Output and Measured Results, $V_g = -3.0, -2.0, -1.0$ and 0.0 V

3.3 SRIM Model

In order to model the proper amount of radiation damage in the AlGaN/GaN-on-Si HEMT, the Monte Carlo ion radiation damage simulator SRIM was utilized . A layered device that has the equivalent dimensions of a two-dimensional slice of the HEMT underneath the gate was designed. These dimensions are found in Table 3.3.

Table 3.3. Device Dimensions Listed from Top to Bottom

Material	Thickness
Si_3N_4	100.0 nm
<i>Au</i> Gate	300.0 nm
<i>Ni</i> Gate	30.0 nm
$Al_{0.27}Ga_{0.73}N$	17.5 nm
<i>GaN</i>	800.0 nm
$Al_{0.4}Ga_{0.6}N$	300.0 nm
$Al_{0.7}Ga_{0.3}N$	400.0 nm
<i>AlN</i>	300.0 nm
Si_3N_4	2.0 nm
<i>Si</i> (111) Substrate	350.0 μ m

After the appropriate dimensions and material names were placed in SRIM, the correct densities were added. For layers that consisted of a monochromatic material, the default density was used. For layers that have specific molar compositions, the density was calculated. The compound correlation value was left at one. The symbols, name, atomic number, weight, atom stoichiometry, Damage Latt and Surf were all left at their default values. The displacement threshold energy values found by Pearton were used [31]. It is noted that while the displacement threshold energy levels for the same atom vary in different compounds, the assumption is made that in GaN, AlGaN, and AlN the thresholds were relatively similar and, therefore, were left as the same. The material properties that were changed can be found in Tables 3.4 and 3.5. The type of TRIM calculation used was a "Detailed Calculation with Full Damage Cascades." The ions used to simulate p⁺ irradiation were hydrogen atoms with the default mass and charge, zero angle of incidence, and 2.0-MeV energy level.

Table 3.4. TRIM Compound Setup Values

Compound	Density (g/cm ³)
<i>Si₃N₄</i>	3.2
<i>Au</i>	19.311
<i>Ni</i>	8.8955
<i>Al_{0.27}Ga_{0.73}N</i>	3.0327
<i>GaN</i>	6.5
<i>Al_{0.4}Ga_{0.6}N</i>	2.8246
<i>Al_{0.7}Ga_{0.3}N</i>	2.3443
<i>AlN</i>	3.26
<i>Si₃N₄</i>	3.44
<i>Si(111)</i>	2.3212

Densities of composite materials were linearly interpolated based on molar composition.

Table 3.5. TRIM Atomic Setup Values

Atoms	Displacement Threshold Energy (eV)
<i>Si</i>	15.0
<i>N</i>	28.0
<i>Au</i>	25.0
<i>Ni</i>	25.0
<i>Al</i>	72.0
<i>Ga</i>	72.0
<i>N</i>	32.4
<i>Si(111)</i>	15.0

Displacement threshold values from [31]

The SRIM program only collects data in 100 bins at a time regardless of the size of the device being modeled. The larger the structure, the wider the bin is required to be, reducing the resolution of the data collected. Due to the size variation of layers within the device, several simulations were run with windows of varying widths. Emphasis was placed on boundary regions and areas where current flows within the device. The following window sizes were utilized in our simulations: 0-3500, 3500-6500, 6500-22475 and 22475-3522500 angstroms. The window size has no effect on the simulation calculations, it merely allows the bin size to be manipulated.

Additional simulations were run at energy levels of 5.0 MeV, 10.0 MeV, 20.0 MeV and 40.0 MeV. Due to the decreasing amount of particle interaction with the lattice as energy level increases, the number of ions simulated increased for increasing energy levels. In order to get accurate information about the interaction of 2.0-MeV proton radiation, 10 million particles were simulated. For 40.0-MeV protons, 50 million particles were simulated.

The resultant damage through irradiation was estimated through measurements of interstitials and vacancies from the materials in each window. Energy levels less than 20.0 MeV showed a linear trend in the interstitial and vacancy formation in both the AlGa_N and GaN regions. The trend was directly correlated to the thickness of the layer. The linear fit for the AlGa_N and GaN regions at 2.0-MeV protons are shown in Tables 3.6, 3.7 and the interstitial distribution in the AlGa_N and GaN regions in Figures 3.14 and 3.15. The 20.0 and 40.0-MeV energy levels showed a constant trend of damage in the lattice. The fitting information for the additional energy levels is found in Appendix, Section A.1.

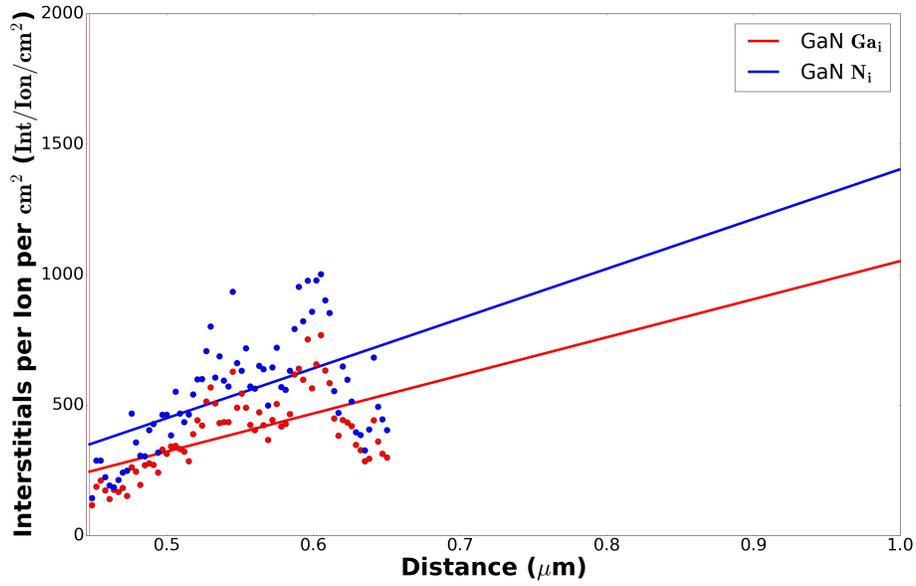


Figure 3.14. Linear Fitting for 2.0-MeV Protons in GaN.

Table 3.6. Interstitial and Vacancy Distribution Fitting Functions in the GaN Region of the Device

Lines for 2.0-MeV energy levels.

Atom	Slope	Y -intercept
Ga_I	1460.437	-408.6899
Ga_V	1439.269	-403.156
N_I	1908.567	-504.769
N_V	1883.116	-500.607

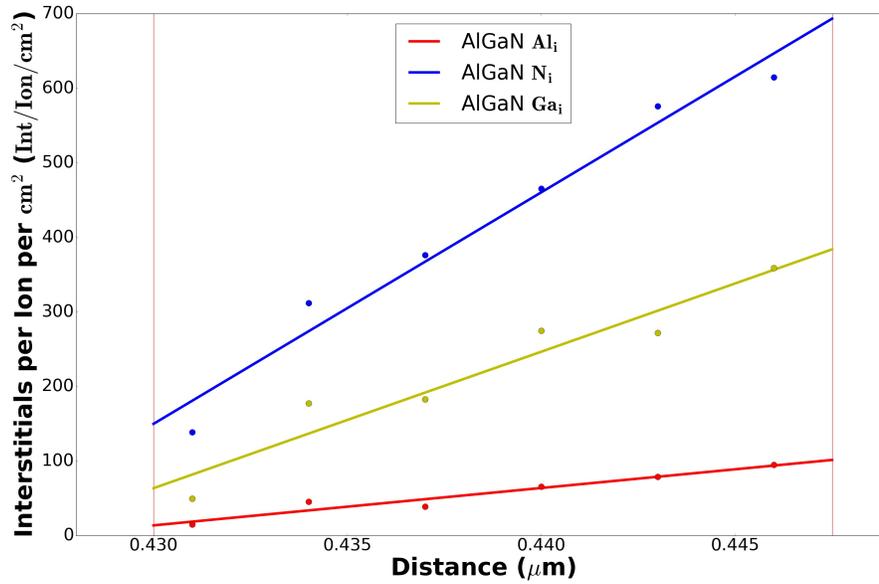


Figure 3.15. Linear Fitting for 2.0-MeV Protons in AlGaN

Table 3.7. Interstitial and Vacancy Distribution Fitting Functions in the AlGaN Region of the Device

Lines for 2.0-MeV energy levels.

Atom	Slope	Y-intercept
Al_I	5015.562	-2143.11
Al_V	4723.538	-2015.279
Ga_I	18310.142	-7809.917
Ga_V	18157.719	-7742.635
N_I	31059.048	-13205.667
N_V	30677.914	-13042.54

CHAPTER 4: Model Implementation

4.1 Impurity Scattering Mobility Implementation

The final piece of the mobility term developed in this work was for the effect of impurity scattering. As stated, our device was not intentionally doped, so an impurity scattering term that is dependent on concentration of dopants returns a value that has no effect on the initial model. Because of this, the tuning of the model to match the characteristics seen in the non-irradiated device was carried out without an impurity dependent term.

To incorporate the effects of impurity scattering in the absence of the first term of Albrecht's mobility equation, the Brooks-Herring model,

$$\frac{1}{\mu_{BH}} = \frac{\alpha\beta T^{\frac{3}{2}}}{N_{imp}} \quad (4.1)$$

was used, where α and β are user defined scaling factors, N_{imp} is the impurity concentration in cm^{-3} and T is the temperature in K. The Brooks Herring model can be shown to provide a more accurate depiction of the impurity dependence of the scattering in a GaN 2DEG [25]; however, the true term should also depend upon the 2DEG density n_{2deg} , which is not included for reasons of convergence. The α and β terms were tuned to be equal to 0.4 and 1.0 so the model would match the measured mobility percent change values in [23]. The result of this fitting is shown in Figure 4.1.

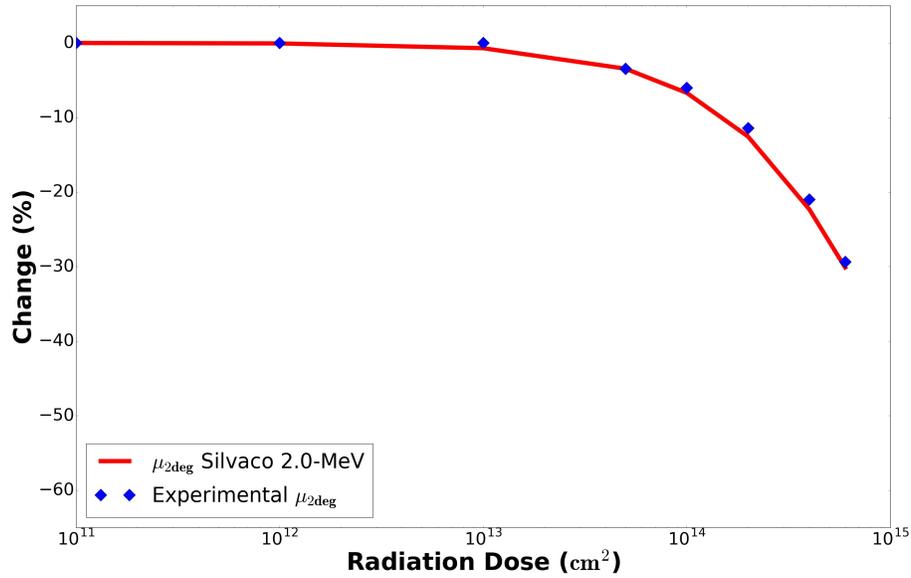


Figure 4.1. Percent Change in μ_{2deg} versus Fluence

The fit for the mobility is almost exact, while the simulation shows an over estimate for all the other properties this study reviewed.

4.2 Model Evaluation Versus 2.0-MeV Experimental Results

The data on the change in characteristics of the HEMT irradiated with 2.0-MeV protons were performed in [26]. In [26] sheet resistance R_{SH} , 2DEG concentration n_{2DEG} , electron mobility μ_{2DEG} , on state resistance R_{on} , transconductance $G_{m,sat}$, threshold voltage V_{th} were measured versus fluence. The experimental results are shown in Figure 4.2.

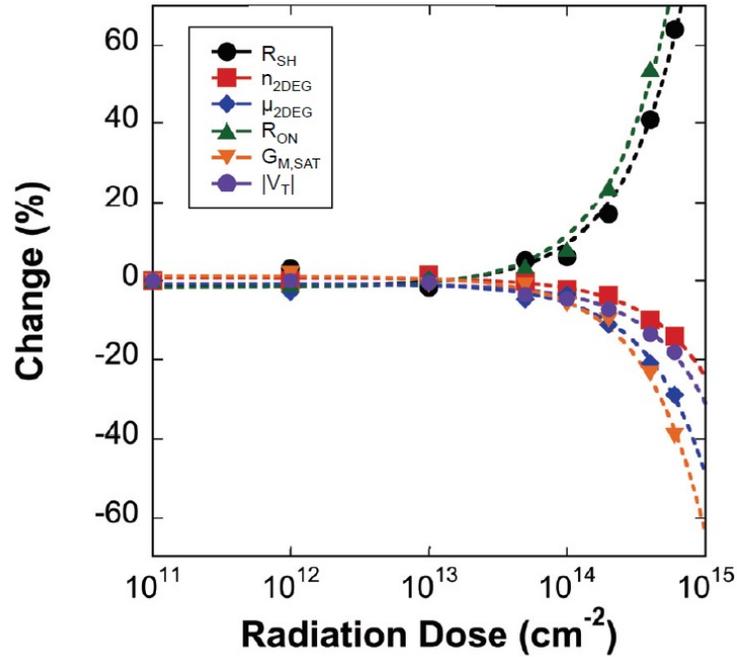


Figure 4.2. Percent Change Values after 2.0-MeV Proton Irradiation. Source: [26].

We matched the fluence levels in [26] for the 2.0-MeV radiation simulation. We compared simulation results to four of the characteristics listed in the key of Figure 4.2: 2DEG electron mobility μ_{2DEG} , threshold voltage V_{th} , on state resistance R_{on} , and transconductance $G_{m,sat}$. The results of the comparison between μ_{2DEG} is shown in Figure 4.1. The comparison between the model outputs and experimental results are laid out in Figures 4.3, 4.4, and 4.5, respectively.

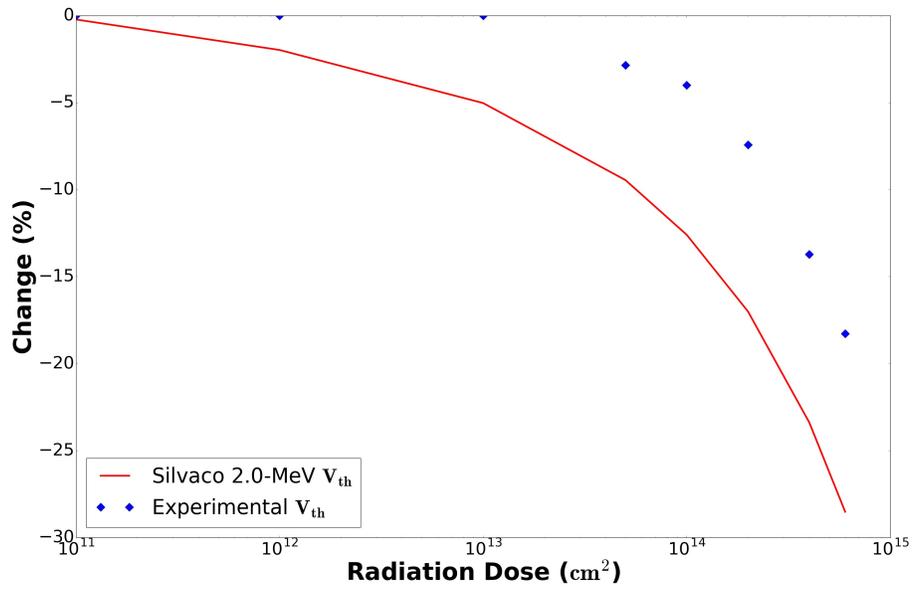


Figure 4.3. Comparison Between Model Output and Experimental Results for Percent Change in V_{th} versus Fluence

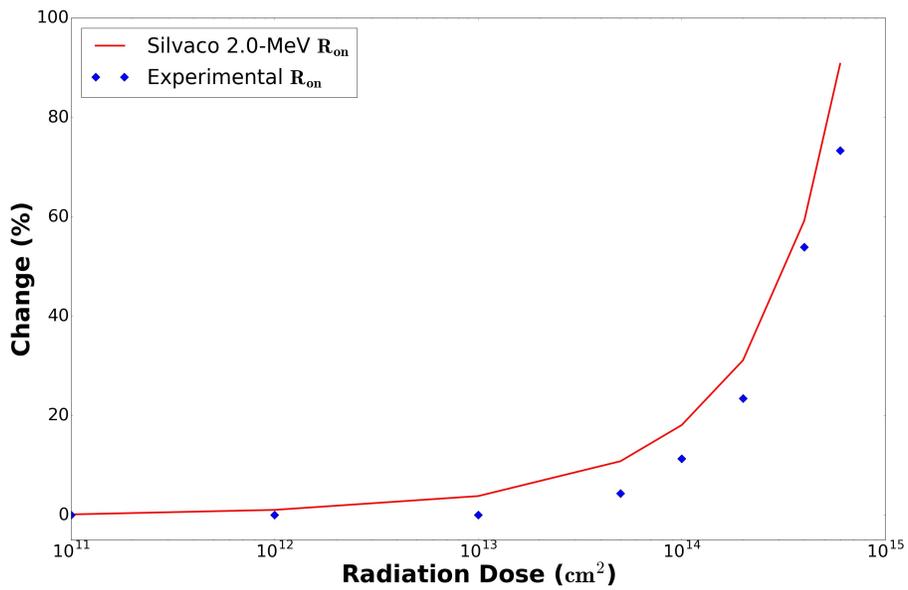


Figure 4.4. Comparison Between Model Output and Experimental Results for Percent Change in R_{on} versus Fluence

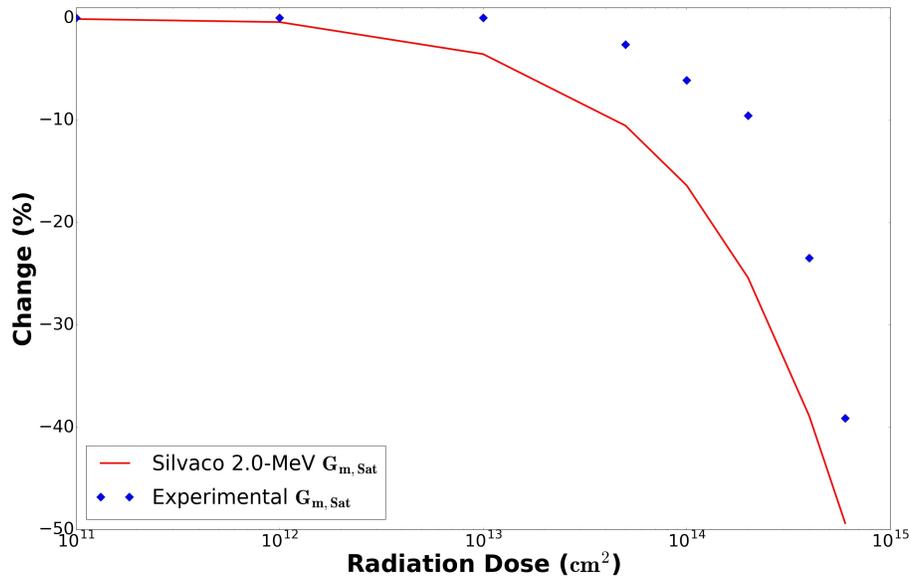


Figure 4.5. Comparison Between Model Output and Experimental Results for Percent Change in $G_{m,sat}$ versus Fluence

From Figures 4.3, 4.4, and 4.5, as stated above, the model overestimates the percent change in comparison to the shifts seen in the physical device. This could be because of the annealing out defects in the physical device. The physical devices were not tested during the radiation event, while the model essentially freezes defects in place and does not allow annealing out. We expect the trap profile to begin to decrease over time as the vacancies and interstitials anneal, reducing the resultant damage. The model does not account for this.

The IV characteristic output by the model after simulated 2.0-MeV proton irradiation to a fluence of $6.0 \times 10^{14} \text{ cm}^{-2}$ are shown in Figures 4.6, 4.7 and 4.8 along with the un-irradiated model outputs. These plots clearly show the threshold voltage shift in the device towards zero at both 100.0 mV and 10.0-V drain voltage values. This matches the results seen in physically radiated devices, discussed further in Section 4.3. We also see the current saturate at a much lower value in the I_d versus V_d curve shown in Figure 4.8, which is something that can easily affect the performance of a component utilizing one of these devices.

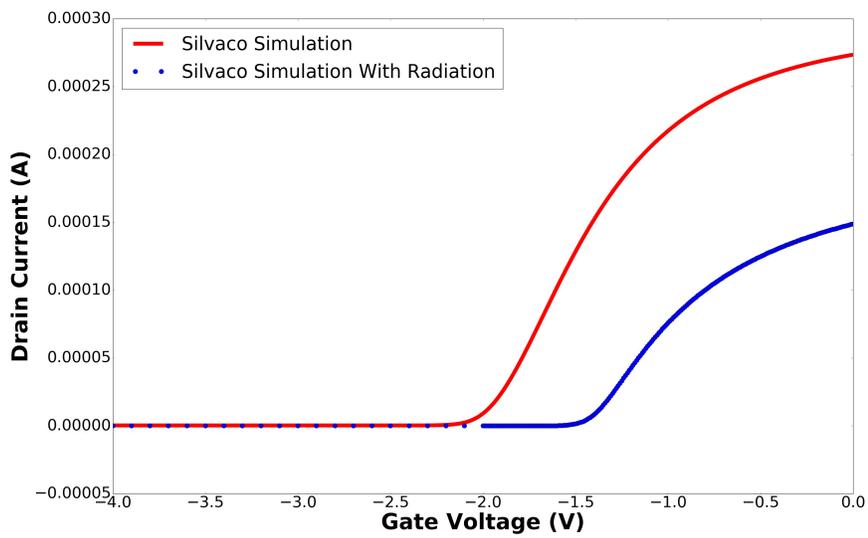


Figure 4.6. V_g versus I_d Comparison, $V_d = 100.0$ mV

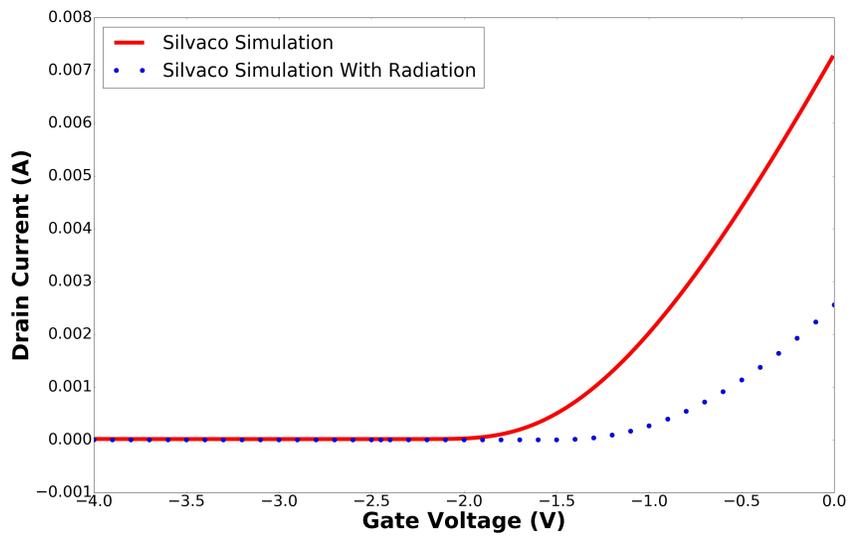


Figure 4.7. V_g versus I_d Comparison, $V_d = 10.0$ V

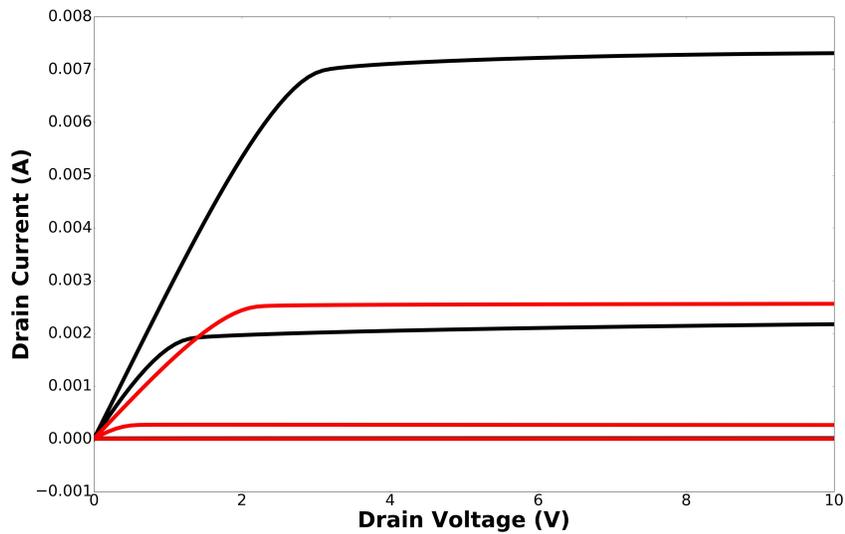


Figure 4.8. I_d versus V_d Comparison, $V_g = -3.0, -2.0, -1.0$ and 0.0 V

4.3 Trap Occupancy and Modulation of the Electric Field

In order to determine the physical origin of the observed shifts in the device characteristics, the internal structure of the device at varying fluence was examined. A review of the structure files produced by the simulation revealed ionized donor and acceptor trap occupancy mismatch in both the GaN and AlGaN regions of the device. This can be seen in Figures 4.9 and 4.10 for the AlGaN region and Figures 4.11 and 4.12 for the GaN region of the device. Both acceptor trap defects maintained higher ionization levels than their donor counterparts.

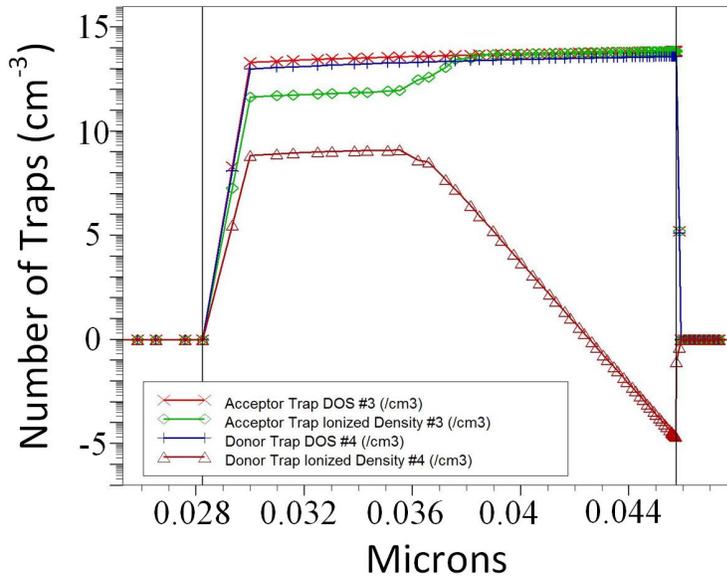


Figure 4.9. Trap and Donor Occupancy Levels (cm^{-3}) in the AlGaIn Barrier Layer at Fluence level of 10^{11}cm^{-2}

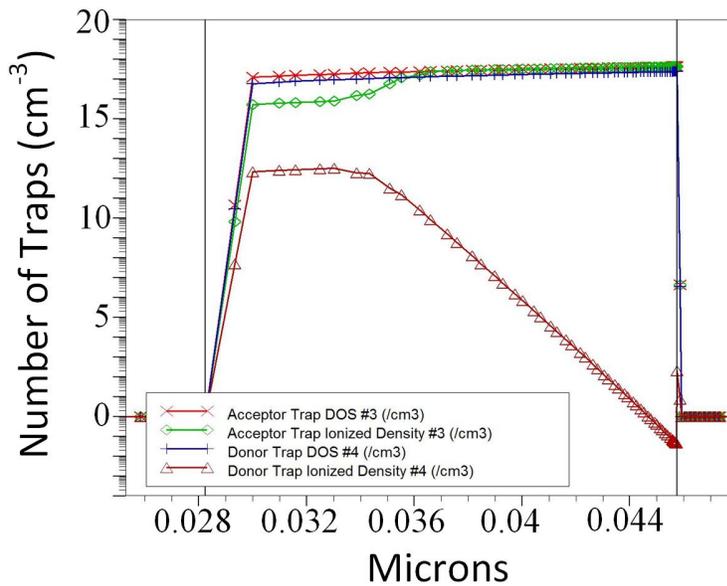


Figure 4.10. Trap and Donor Occupancy Levels (cm^{-3}) in the AlGaIn Barrier Layer at Fluence level of $6.0 \times 10^{14} \text{cm}^{-2}$

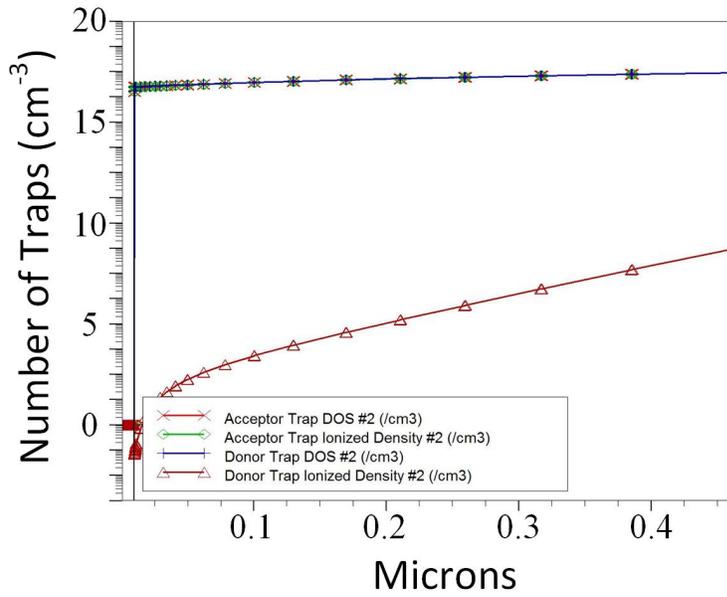


Figure 4.11. Trap and Donor Occupancy Levels (cm^{-3}) in the GaN Barrier Layer at Fluence level of 10^{11} cm^{-2}

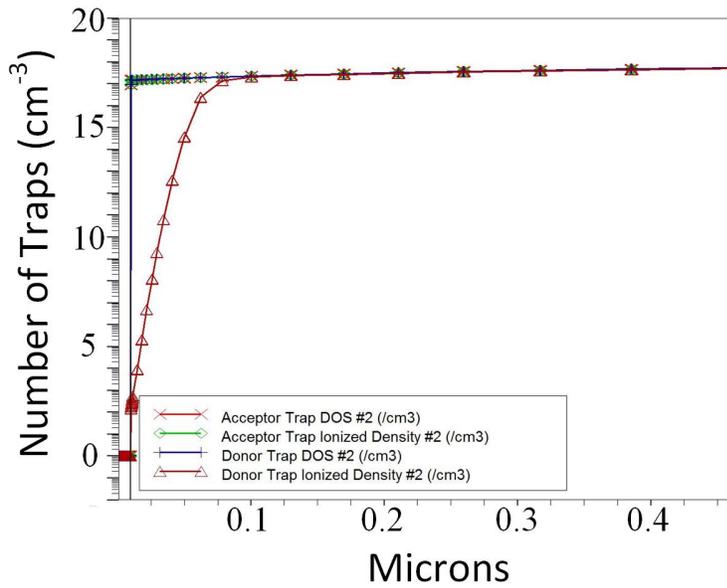


Figure 4.12. Trap and Donor Occupancy Levels (cm^{-3}) in the GaN Barrier Layer at Fluence level of $6.0 \times 10^{14} \text{ cm}^{-2}$

The trap and donor ionization difference creates a build up of negative charge in the AlGaN and GaN regions of the device. This charge buildup screens out the generation of the 2DEG, which results in the threshold voltage shift towards zero. After radiation, less charge is needed to turn the device off as the 2DEG is not as concentrated, resulting in decreased current for a given bias condition and decreased transconductance.

The second effect is seen in the spread of the electric field, as shown in Figures 4.13 and 4.14. The electric field under the gate on the drain side of the device spreads out over a larger area at higher fluence levels. This increase in width decreases the field and increases the breakdown voltage of the device. The effect on the field under the drain edge of the gate can be seen more quantitatively in Figure 4.15, where the field under the drain side of the gate is shown.

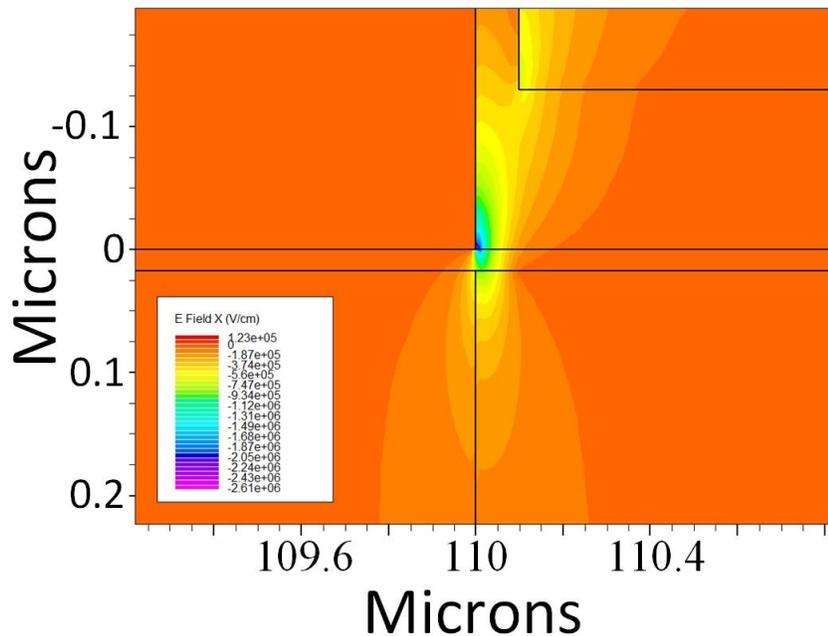


Figure 4.13. Electric Field Distribution at a Fluence of 10^{11} cm^{-2}

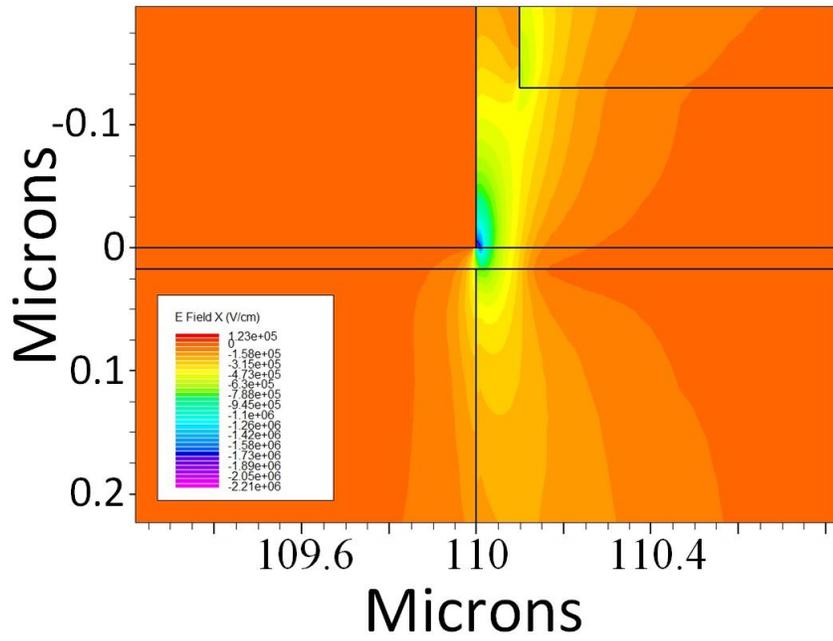


Figure 4.14. Electric Field Distribution at a Fluence of $6.0 \times 10^{14} \text{cm}^{-2}$

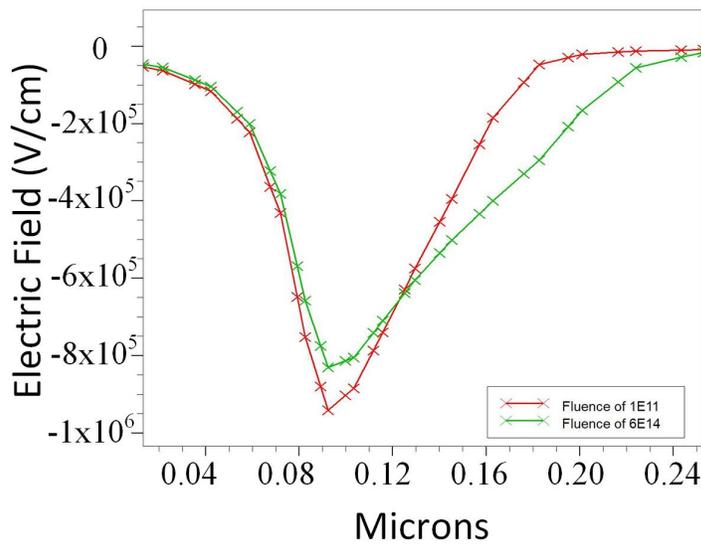


Figure 4.15. Electric Field Distribution at Fluences of 10^{11}cm^{-2} and $6.0 \times 10^{14} \text{cm}^{-2}$

4.4 Model Evaluation at Additional Energy Levels

Using the additional radiation profiles derived from SRIM, we predicted the effects that might be seen in an actual radiation event at 5.0, 10.0, 20.0 and 40.0 MeV to similar fluence levels. The comparison between the percent change in key device characteristics and proton energy levels can be seen in Figures 4.16, 4.17, 4.18 and 4.19. The idea that the higher the energy level of the proton the more fluence is required to inflict a similar amount of damage to the device was expected to hold; however, the increase in fluence needed to shift device characteristics by a similar amount decreases as particle energy level increases. This is unexpected, as decreasing particle interaction should make it harder to damage the device. As the particle energy increases, we expect to see fewer interactions with lattice atoms, but when interactions occur, the results will be more extreme than at lower energy levels. Again, this is an issue of transferred energy. A 40.0-MeV proton has a lot more energy to transfer to a PKA than a 5.0-MeV proton. Where a 5.0-MeV proton may knock three atoms from their original location, a 40.0-MeV proton can knock out 50. Also, if an event occurs with a higher energy level proton, the proton now has less energy and chances of interacting with other particles increase.

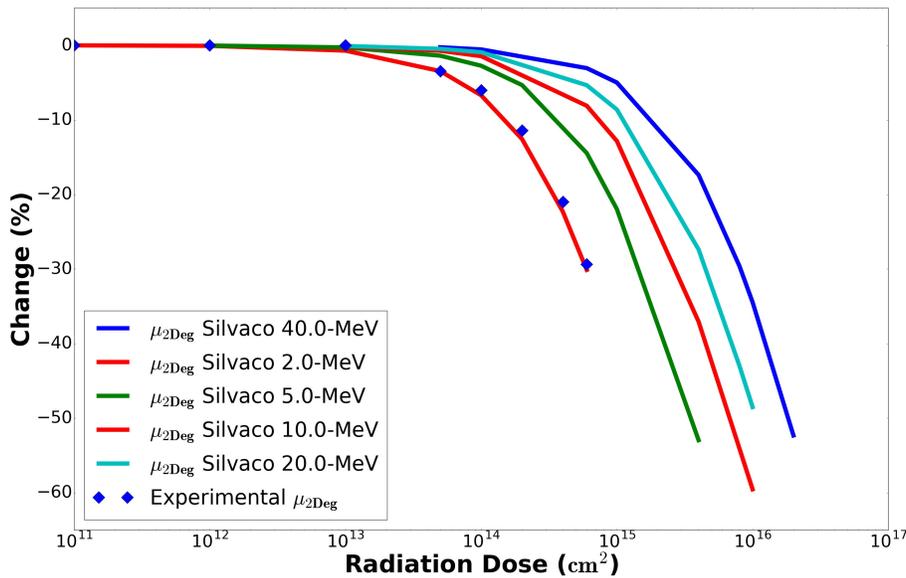


Figure 4.16. Percent Change in μ_{2deg} versus Fluence for Varying Proton Energies

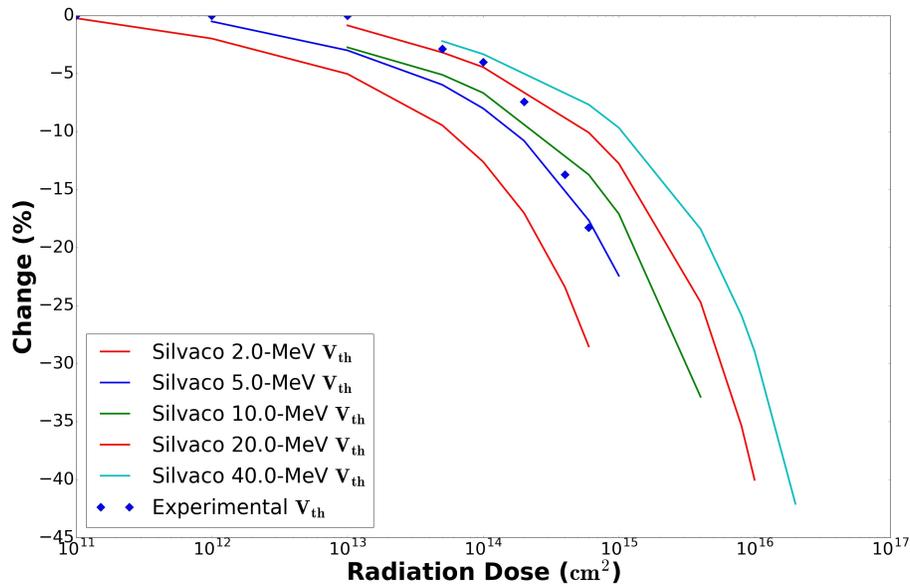


Figure 4.17. Percent Change in V_{th} versus Fluence for Varying Proton Energies

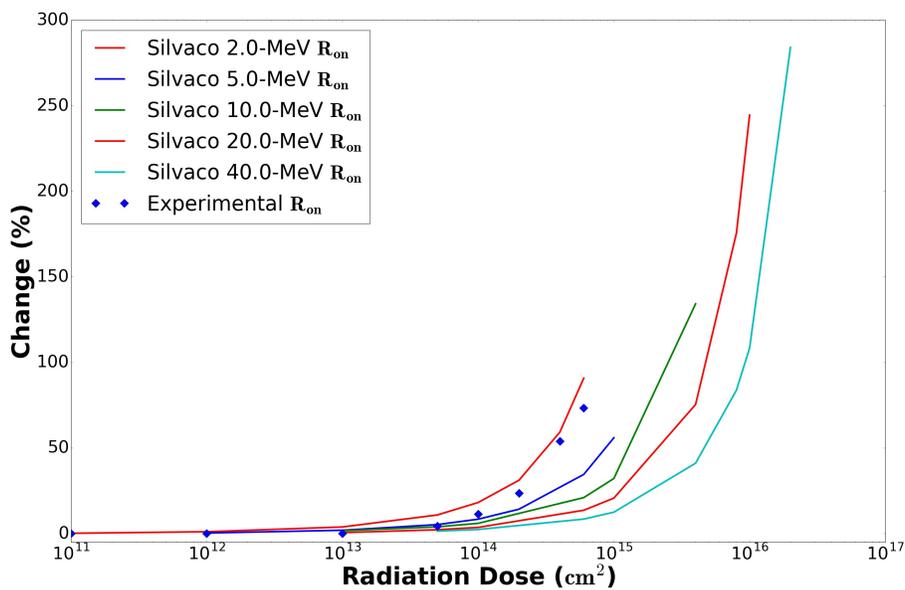


Figure 4.18. Percent Change in R_{on} versus Fluence for Varying Proton Energies

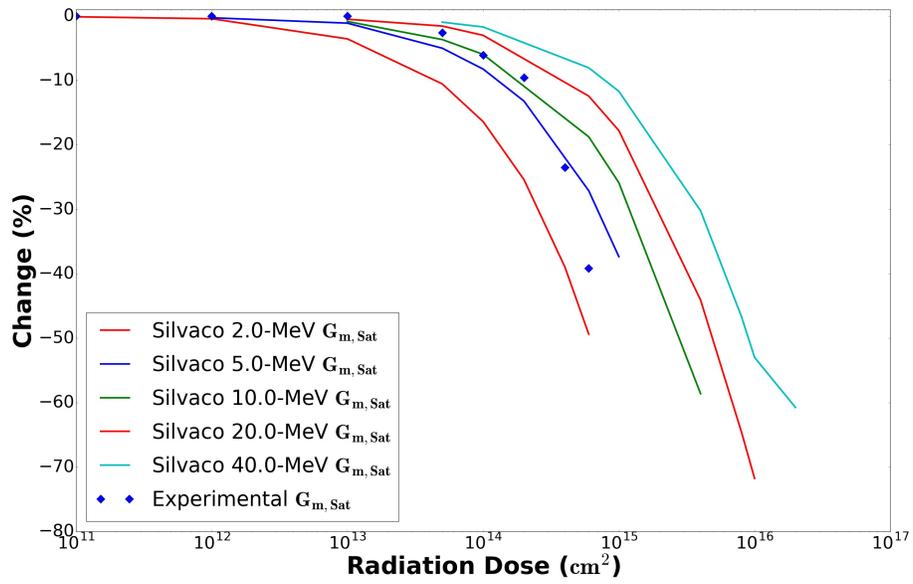


Figure 4.19. Percent Change in $g_{m,sat}$ versus Fluence for Varying Proton Energies

CHAPTER 5: Conclusions

In this study, we have successfully created a TCAD model that utilizes Monte Carlo simulated proton irradiation damage levels for several different proton energy levels while incorporating a customized calculation for the electron mobility in the 2DEG to simulate high-dose proton irradiation in a GaN-on-Si HEMT.

Generally, the model over-predicted the damage that was observed in previous NPS and NRL experimental work. We did not over-predict the mobility shift in radiated devices because the mobility was used to tune the coefficients in the customized mobility calculation. One issue with using this metric to tune the model is that the devices that were physically tested were not immediately characterized after irradiation. This allows the device time to anneal out defects that formed during the irradiation. This can result in a shift back to less damage in the device. The model effectively freezes the defects in place in the lattice without any function to allow for them to anneal; however, the model provides a good baseline model for the exploration of radiation damage in GaN-on-Si HEMTs.

Continued research into GaN-on-Si devices is vital to the Department of Defense (DoD) as more and more hardware systems adopt these HEMTs. They strengthen our equipment, but the most important part of strength is knowing weaknesses. This research increases our understanding of these powerful devices that are now being utilized in active systems.

5.0.1 Future Work

The Silvaco software does not have specialized formulas which depend upon 2DEG mobility such as those proposed in research by Lisesivdin [25]. For future work on this project, more physically exact terms for mobility should be incorporated, such as the effects of roughness scattering. For the HEMTs that were used in this study, prior work by Greenlee [32] documented the visible shift in atoms at the boundary layer between the AlGaN and GaN layers, which has an effect on the 2DEG in that region through roughness scattering. Additional research should also examine various ways to model the electron mobility shift caused by PCF without physically altering the model. More research is also needed in

this simulation to model the diffusion of defects throughout the lattice in order to identify mechanisms for void sinks causing defects like the voiding seen under the gate of the device by Wade [10]. Lastly, work by Pearton identified different defect types created by different energy levels of proton radiation. Additional research should be devoted to identifying these trap levels and incorporating them into models for specific energy levels of proton irradiation. This model can serve as a valuable tool for predicting the effects in the experiments that should follow, 40.0-MeV proton irradiation of NRL GaN-on-Si HEMTs to fluence levels greater than 10^{15}cm^{-2} . This tool will also prove valuable for upcoming neutron irradiation testing.

APPENDIX

A.1 SRIM Simulation Values

Table A.1. Interstitial and Vacancy Fitting Functions in the GaN Region of the Device

Atom	Slope ($(defects/cm)/(ion/\mu m)$)	Y-intercept
Ga_I	395.816	-83.213
Ga_V	648.499	-198.918
N_I	402.650	-35.729
N_V	841.037	-244.639

5.0-MeV Protons

Table A.2. Interstitial and Vacancy Fitting Functions in the AlGaN Region of Device

Atom	Slope ($(defects/cm)/(ion/\mu m)$)	Y-intercept
Al_I	918.307	-388.069
Al_V	102.064	-19.034
Ga_I	4299.410	-1816.631
Ga_V	2817.0904	-1117.765
N_I	10080.524	-4296.504
N_V	2837.467	-1042.749

5.0-MeV Protons

Table A.3. Interstitial and Vacancy Fitting Functions in the GaN Region of the Device

Atom	Slope $((defects/cm)/(ion/\mu m))$	Y -intercept
Ga_I	315.347	-91.402
Ga_V	310.406	-89.853
N_I	437.557	-123.811
N_V	432.481	-123.114

10.0-MeV Protons

Table A.4. Interstitial and Vacancy Fitting Functions in the AlGaN Region of Device

Atom	Slope $((defects/cm)/(ion/\mu m))$	Y -intercept
Al_I	473.033	-193.481
Al_V	453.97	-185.344
Ga_I	2358.752	-983.149
Ga_V	2034.923	-840.816
N_I	3345.905	-1365.073
N_V	2752.402	-1105.875

10.0-MeV Protons

Table A.5. Interstitial and Vacancy Fitting Functions in the GaN Region of the Device

Atom	Slope $((defects/cm)/(ion/\mu m))$	Y -intercept
Ga_I	0	31.988
Ga_V	0	31.968
N_I	0	45.575
N_V	0	45.085

20.0-MeV Protons

Table A.6. Interstitial and Vacancy Fitting Functions in the AlGa_N Region of Device

Atom	Slope $((defects/cm)/(ion/\mu m))$	Y-intercept
Al_I	276.451	-112.589
Al_V	400.732	-166.478
Ga_I	1258.994	-520.669
Ga_V	1550.988	-647.579
N_I	949.152	-352.061
N_V	1454.471	-572.491

20.0-MeV Protons

Table A.7. Interstitial and Vacancy Fitting Functions in the GaN Region of the Device

Atom	Slope $((defects/cm)/(ion/\mu m))$	Y-intercept
Ga_I	0	17.561
Ga_V	0	17.238
N_I	0	25.968
N_V	0	25.489

40.0-MeV Protons

Table A.8. Interstitial and Vacancy Fitting Functions in the AlGa_N Region of Device

Atom	Slope $((defects/cm)/(ion/\mu m))$	Y-intercept
Al_I	-79.039	40.018
Al_V	-128.416	61.496
Ga_I	681.631	-282.472
Ga_V	686.527	-284.880
N_I	790.314	-310.940
N_V	844.579	-335.516

40.0-MeV Protons

A.2 SILVACO Simulation Values

Table A.9. Albrecht Model Values. Adapted from [33]

A_N	0
B_N	5
C_N	0.4
N_0	10^{17}
T_0	300.0
T_1	1065.0

Values A, B and C were calculated based on μ_n of 1265 from [34] with A constantly zero.

A.3 Trap Levels in GaN

Table A.10. Defects Introduced by Various Types of Irradiation in GaN. Adapted from [20].

Material type, dopant concentration (cm^{-3})	Radiation type	Carrier removal rate, (cm^{-1})	Defect levels (activation energy (eV) from conduction C or Valence V), defect type (donor D, acceptor A)	Defect production rate (cm^{-1})	Proposed identity
n-GaN, 10^{16}	Protons, 2 MeV	260	0.13, C, ? 0.16, C, ? 0.2, C, A	30 400 600	ER1 ER2 ER2
n-GaN, 10^{16}	Protons, 150 keV	100	0.2, C, ? 0.25, C, ? 0.32, C, ? 0.45, C, ? 0.6, C, A 0.8, C, D		ER3 Complex of ER3 Complex of ER3 Complex of ER3 Ga_i

Table A.11. Stated Energy Levels for Defects in GaN. Adapted from [20].

Atom	Vacancy or Interstitial	Acceptor or Donor	Deep or Shallow	Energy Level
Ga	Interstitial	Donor	Deep	$E_c - 0.8 \text{ eV}$
Ga	Vacancy	Acceptor	Deep	$E_v + 1.0 \text{ eV}$
N	Interstitial	Acceptor	Deep	$E_c - 1.0 \text{ eV}$
N	Vacancy	Donor	Shallow	$E_c - 0.06 \text{ eV}$

A.4 Code

A.4.1 Silvaco Deckbuild Code

```
go atlas simflags="-P 12"
```

```
set radenergy = 2
set fluence = 6e14
set talgan = 17.5e-3
set tgan = 0.8
set talgan2 = 0.517+0.258
set taln = 0.427
set tsi = 350
set tni = 0.03
set taug = 0.3
set tausd = 0.33
set tsin = 0.133
set tair = 0.366
set lsin = .133
```

```
set lgate = 7
set ls = 100
set lsg = 3
set lgd = 13
set ld = 100
```

```
set Tem = 21
```

set pz = 7.2e12

mesh width=100

x.mesh location=0 spacing=\$ls/5
x.mesh location=\$ls spacing=\$ls/100
x.mesh location=\$ls+0.5*\$lsg spacing=\$lsg/10
x.mesh location=\$ls+\$lsg-0.1 spacing=\$lgate/18
x.mesh location=\$ls+\$lsg spacing=\$lgate/70
x.mesh location=\$ls+\$lsg+0.5*\$lgate spacing=\$lgate/10
x.mesh location=\$ls+\$lsg+\$lgate spacing=\$lgate/700
x.mesh location=\$ls+\$lsg+\$lgate+0.1 spacing=0.02
x.mesh location=\$ls+\$lsg+\$lgate+0.5*\$lgd spacing=\$lgd/10
x.mesh location=\$ls+\$lsg+\$lgate+\$lgd spacing=\$ld/100
x.mesh location=\$ls+\$lsg+\$lgate+\$lgd+\$ld spacing=\$ld/5

y.mesh location=-1*(\$tni+\$taug+\$tsin) spacing=\$tsin/2
y.mesh location=-1*(\$tausd) spacing=\$tausd/10
y.mesh location=-1*(\$tni) spacing=\$tni/10
y.mesh location=0 spacing=\$talgan/10
y.mesh location=0.99*\$talgan spacing=\$talgan/100
y.mesh location=0.999*\$talgan spacing=\$talgan/1000
y.mesh location=\$talgan spacing=\$talgan/100
y.mesh location=\$talgan+0.002*\$tgan spacing=\$tgan/250
y.mesh location=\$talgan+0.02*\$tgan spacing=\$tgan/200
y.mesh location=\$talgan+0.2*\$tgan spacing=\$tgan/20
y.mesh location=\$talgan+\$tgan spacing=\$tgan/6
y.mesh location=\$talgan+\$tgan+\$talgan2 spacing=\$talgan2/5
y.mesh location=\$talgan+\$tgan+\$talgan2+\$taln spacing=1
y.mesh location=\$talgan+\$tgan+\$talgan2+\$taln+\$tsi spacing=\$tsi/4

region number=1 material=AlGaN x.mole=0.27 x.min=0 x.max=\$ls+\$lsg+\$lgate+\$lgd+\$ld
y.min=0 y.max=\$talgan
region number=2 material=GaN substrate x.min=0 x.max=\$ls+\$lsg y.min=\$talgan

y.max=\$talgan+\$tgan
region number=3 material=AlGaIn x.mole=0.7 y.min=\$talgan+\$tgan
y.max=\$talgan+\$tgan+\$talgan2
region number=4 material=AlN x.min=0 x.max=\$ls+\$lsg+\$lgate+\$lgd+\$ld
y.min=\$talgan+\$tgan+\$talgan2 y.max=\$talgan+\$tgan+\$talgan2+\$taln
region number=5 material=Si x.min=0 x.max=\$ls+\$lsg+\$lgate+\$lgd+\$ld
y.min=\$talgan+\$tgan+\$talgan2+\$taln y.max=\$talgan+\$tgan+\$talgan2+\$taln+\$tsi

region number=6 material=gold x.min=0 x.max=\$ls y.min=-1*\$tausd y.max=0
region number=7 material=nitride x.min=\$ls x.max=\$ls+\$lsg y.min=-1*\$tsin y.max=0
region number=7 material=nitride x.min=\$ls+\$lsg-0.1 x.max=\$ls+\$lsg
y.min=-1*(\$tni+\$taug+\$tsin) y.max=-1*\$tsin
region number=7 material=nitride x.min=\$ls+\$lsg+\$lgate x.max=\$ls+\$lsg+\$lgate+0.1
y.min=-1*(\$tni+\$taug+\$tsin) y.max=-1*\$tsin
region number=7 material=nitride x.min=\$ls+\$lsg x.max=\$ls+\$lsg+\$lgate
y.min=-1*(\$tni+\$taug+\$tsin) y.max=-1*(\$tni+\$taug)
region number=7 material=nitride x.min=\$ls+\$lsg+\$lgate
x.max=\$ls+\$lsg+\$lgate+\$lgd y.min=-1*\$tsin y.max=0
region number=8 material=nickel x.min=\$ls+\$lsg x.max=\$ls+\$lsg+\$lgate
y.min=-1*\$tni y.max=0
region number=9 material=gold x.min=\$ls+\$lsg x.max=\$ls+\$lsg+\$lgate
y.min=-1*(\$tni+\$taug) y.max=-1*\$tni

region number=11 material=gold x.min=\$ls+\$lsg+\$lgate+\$lgd
x.max=\$ls+\$lsg+\$lgate+\$lgd+\$ld y.min=-1*\$tausd y.max=0
region number=12 material=GaIn x.min=\$ls+\$lsg x.max=\$ls+\$lsg+\$lgate
y.min=\$talgan y.max=\$talgan+\$tgan
region number=13 material=GaIn x.min=\$ls+\$lsg+\$lgate
x.max=\$ls+\$lsg+\$lgate+\$lgd+\$ld y.min=\$talgan y.max=\$talgan+\$tgan
region number=14 material=air x.min=\$ls x.max=\$ls+\$lsg-0.1
y.min=-1*(\$tni+\$taug+\$tsin) y.max=-1*\$tsin
region number=14 material=air x.min=0 x.max=\$ls y.min=-1*(\$tsin+\$tausd)
y.max=-1*(\$tausd)
region number=15 material=air x.min=\$ls+\$lsg+\$lgate+0.1
x.max=\$ls+\$lsg+\$lgate+\$lgd y.min=-1*(\$tni+\$taug+\$tsin) y.max=-1*\$tsin

```
region number=15 material=air x.min=$ls+$lsg+$lgate+$lgd
x.max=$ls+$lsg+$lgate+$lgd+$ld y.min=-1*($tsin+$tausd) y.max=-1*($tausd)
```

```
electrode name=gate x.min=$ls+$lsg x.max=$ls+$lsg+$lgate y.min=-1*$tausd y.max=0
electrode name=source x.min=0 x.max=$ls y.min=-1*$tausd y.max=0
electrode name=drain x.min=$ls+$lsg+$lgate+$lgd x.max=$ls+$lsg+$lgate+$lgd+$ld
y.min=-1*$tausd y.max=0
electrode name=substrate bottom
```

```
doping n.type conc=1e18 uniform x.min=0 x.max=$ls y.min=0 y.max=$talgan
doping n.type conc=1e18 uniform x.min=$ls+$lsg+$lgate+$lgd
x.max=$ls+$lsg+$lgate+$lgd+$ld y.min=0 y.max=$talgan
```

```
doping f.doping="GaN_N_I.lib" trap acceptor e.level=1.0 degen.fac = 2
sign=1e-15 sigp=1e-15
doping f.doping="GaN_N_V.lib" trap donor e.level=3.34 degen.fac = 2
sign=1e-15 sigp=1e-15
doping f.doping="GaN_Ga_V.lib" trap acceptor e.level=2.4 degen.fac = 2
sign=1e-15 sigp=1e-15
doping f.doping="GaN_Ga_I.lib" trap donor e.level=2.6 degen.fac = 2
sign=1e-15 sigp=1e-15
```

```
doping f.doping="AlGaN_N_I.lib" trap acceptor e.level=1.0 degen.fac = 2
sign=1e-15 sigp=1e-15
doping f.doping="AlGaN_N_V.lib" trap donor e.level=3.34 degen.fac = 2
sign=1e-15 sigp=1e-15
doping f.doping="AlGaN_Ga_V.lib" trap acceptor e.level=2.4 degen.fac = 2
sign=1e-15 sigp=1e-15
doping f.doping="AlGaN_Ga_I.lib" trap donor e.level=2.6 degen.fac = 2
sign=1e-15 sigp=1e-15
```

```
#doping f.doping="AlGaN_Al_V.lib" trap acceptor? e.level=2.4? degen.fac = 2
sign=1e-15 sigp=1e-15 region=5
#doping f.doping="AlGaN_Al_I.lib" trap donor? e.level=2.6? degen.fac = 2
```

sign=1e-15 sigp=1e-15 region=5

#Values taken from 8-3, 8-4 from pg 534 of atlas users manual using GaN/2 and AlN/2 values from CH6 of the users manual. Exponent term was not halved.

material region=1 affinity=3.6 tcon.power tc.npow = .317 tc.const = 1.381

material region=2 affinity=3.932 tcon.power tc.npow = .28 tc.const = .65

material region=3 affinity=2.78 tcon.power tc.const = 1.5535 tc.npow = .688

material region=4 affinity=2.03 tcon.power tc.npow = 1.64 tc.const = 1.425

material region=5 affinity=4.05 tcon.power tc.const = 1.48

material region=6 tcon.power tc.const = 2.0

material region=8 tcon.power tc.const = 1.58

material region=12 affinity=3.932 tcon.power tc.npow = .28 tc.const = .65

material region=13 affinity=3.932 tcon.power tc.npow = .28 tc.const = .65

contact name=gate work=4.6 surf.rec

contact name=source work=3.6 resistance=10

contact name=drain work=3.6 resistance=10

models print k.p fermi srh

models lat.temp heat.full

interface charge=\$pz s.s y.min=\$talgan y.max=\$talgan

thermcontact number=1 elec.number=4 temperature=273.15+\$Tem

mobility region=2 f.tofimun="Mob0.lib"

mobility region=12 f.tofimun="Mob1.lib"

mobility region=13 f.tofimun="Mob2.lib"

output con.band val.band charge int.charge polar.charge e.mobility

method block newton itlimit=25 maxtraps=20 nblockit=100 carriers=2

A.4.2 Tofimun Mobility Code

GaN Region 0

```
#include <stdio.h>
#include <stdlib.h>
#include <math.h>
#include <ctype.h>
#include <malloc.h>
#include <string.h>
#include <template.h>

/*
 * -----
 * ATLAS Parser Function Template
 * ATLAS Version 5.21.1.C
 * c 1993 - 2015 SILVACO Inc.
 * All rights reserved.
 * -----
 */

/*
 * General field dependent mobility model for electrons.
 * TOfimun FIeld Mobility (parallel and perpendicular field components)
 * Statement: MATERIAL/MOBILITY
 * Parameter: F.TOFIMUN
 * Arguments:
 * Eperp    [in] - perpendicular electric field (V/cm)
 * Na       [in] - acceptor concentration (/cm^3)
 * Nd       [in] - donor concentration (/cm^3)
 * nconc    [in] - electron concentration (/cm^3)
 * Eparl    [in] - parallel electric field (V/cm)
 * TL       [in] - lattice temperature (K)
 * xcomp    [in] - x-species fraction (0-1)
 * ycomp    [in] - y-species fraction (0-1)
 *

```

```

* *mun      [return] - hole mobility (cm2/Vs)
* *dmundep  [return] - derivative of *mun wrt Eperp
* *dmundeparl [return] - derivative of *mun wrt Eparl
* *dmundl   [return] - derivative of *mun wrt TL
* *dmundn   [return] - derivative of *mun wrt nconc

```

```
*/
```

```

int tofimun(double Eperp,double Na,double Nd,double nconc,double Eparl,
double TL,double xcomp,double ycomp,double *mun,double *dmundep,
double *dmundepar,double *dmundl,double *dmundn)
{
double A=0.25*2.61e-4, B=4*2.9e-4, C=4*170e-4, N0n=1e17, T0n=300.0, t1n=1065.0,
alpha=0.4,beta = 1.0,Ecrit=20e3 ,N1=2.0 ,Vsat=3e7;
double invmu,DD0,DD1,DD2,invmuALB,h,g,hPrime,gPrime,MuField;
double N_imp=Na+Nd;
invmuALB=A*(N_imp/N0n)*pow(TL/T0n,-1.5)+B*pow((TL/T0n),1.5)+C*pow((exp(t1n/TL)-1),-1);
DD0=-1.5*A*(N_imp/N0n)*pow(TL/T0n,-2.5);
DD1=B*(1.5)*pow((TL/T0n),0.5)*(1/T0n);
DD2=C*t1n*pow((exp(t1n/TL)-1),-2)*(pow(TL,-2));

invmu=invmuALB;

h=1+pow((Eparl/Ecrit),N1);
hPrime=(N1/pow(Ecrit,N1))*pow(Eparl,(N1-1));
g=(1/invmu)+Vsat*(pow(Eparl,(N1-1))/pow(Ecrit,N1));
gPrime=(Vsat/pow(Ecrit,N1))*(N1-1)*pow(Eparl,(N1-2));

MuField=g/h;

*mun = MuField;
*dmundepar = 0;
//(gPrime/h)-(1/invmu)*(hPrime/h);
*dmundep=0.0;

```



```

*dmundl =(DD0+DD1+DD2)/(invmu*invmu)/h;
*dmundn = 0/(invmu*invmu)/h;

return(0);

```

GaN Region 1

Code is the same as seen in GaN Region 0 with the constant values changed. Only the constant values have been listed here.

```

double A=0.25*2.61e-4, B=1.35*2.9e-4, C=1.35*170e-4, N0n=1e17, T0n=300.0, t1n=1065.0,
alpha=0.4,beta = 1.0, Ecrit=20e3, N1=2, Vsat=3e7;

```

GaN Region 2

Code is the same as seen in GaN Region 0 with the constant values changed. Only the constant values have been listed here.

```

double A=0.25*2.61e-4, B=2*2.9e-4, C=2*170e-4, N0n=1e17, T0n=300.0, t1n=1065.0,
alpha=0.4,beta = 1.0, Ecrit=20e3 ,N1=2.0 ,Vsat=3e7;

```

A.4.3 Vacancy / Interstitial Formation Code

AlGaN AI Interstitial Code

```

#include <stdio.h>
#include <stdlib.h>
#include <math.h>
#include <ctype.h>
#include <malloc.h>
#include <string.h>
#include <template.h>

```

```

/*

```

```

* -----

```

```

* ATLAS Parser Function Template
* ATLAS Version 5.21.1.C
* c 1993 - 2015 SILVACO Inc.
* All rights reserved.
* -----
*/
/*
* Position dependent net doping.
* Statement: DOPING
* Parameter: F.DOPING
* Arguments:
* x      location x (microns)
* y      location y (microns)
* *nnet  net doping concentration (per cc)
*/
int doping(double x,double y,double *nnet)
{
double talgan = 0.0175;
double tgan = 0.8;
if(y<0){
*nnet = 0;
}
else if(y>=0 && y<=talgan){
double flu=8e+14;
*nnet= flu*5015.561905*(y+0.43)-2143.1099108;
}
else{
*nnet=0;
}

return(0);
}

```

THIS PAGE INTENTIONALLY LEFT BLANK

List of References

- [1] J. Zolper, “Delivering discriminating technologies,” *Technology Today*, vol. 1, no. 1, pp. 4–7, 2014.
- [2] C. Whelan, N. Koliass, J. Smolko, T. Kazior, and S. Bernstein, “State-of-the-art RF semiconductors,” *Technology Today*, vol. 1, no. 1, pp. 14–17, 2014.
- [3] M. Sarcione, P. Hull, C. Whelan, D. Tonomura, T. V. Sikina, J. Wilson, and R. E. D. II, “Past, present and future,” *Technology Today*, vol. 1, no. 1, pp. 8–13, 2014.
- [4] X. Hu, A. P. Karmarkar, B. Jun, D. M. Fleetwood, R. D. Schrimpf, R. D. Geil, R. A. Weller, B. D. White, M. Bataiev, and L. J. Brillson, “Proton-irradiation effects on algan/aln/gan high electron mobility transistors,” *IEEE Transactions on Nuclear Science*, vol. 50, no. 6, pp. 1791–1796, 2003.
- [5] X. Hu, B. K. Choi, H. J. Barnaby, D. M. Fleetwood, R. D. Schrimpf, S. Lee, S. Shojah-Ardalan, R. Wilkins, U. K. Mishra, and R. W. Dettmer, “The energy dependence of proton-induced degradation in algan/gan high electron mobility transistors,” *IEEE Transactions on Nuclear Science*, vol. 51, no. 2, pp. 293–297, 2004.
- [6] G. Sonia, F. Brunner, A. Denker, R. Lossy, M. Mai, J. Opitz-Coutureau, G. Pensl, E. Richter, J. Schmidt, and U. Zeimer, “Proton and heavy ion irradiation effects on algan/gan hfet devices,” *IEEE Transactions on Nuclear Science*, vol. 53, no. 6, pp. 3661–3666, 2006.
- [7] H.-C. Yu, “Rigorous model and simulations of the kirkendall effect diffusion in substitutional binary alloys,” Ph.D. dissertation, Illinois Institute of Technology, 2009.
- [8] A. Kalavagunta, M. Silvestri, M. Beck, S. Dixit, R. D. Schrimpf, R. Reed, D. Fleetwood, L. Shen, and U. Mishra, “Impact of proton irradiation-induced bulk defects on gate-lag in gan hemts,” *IEEE Transactions on Nuclear Science*, vol. 56, no. 6, pp. 3192–3195, 2009.
- [9] D. A. Cary, “Ionizing radiation tolerance of a gallium nitride power transistor,” Master’s thesis, Monterey, California: Naval Postgraduate School, 2013.

- [10] M. G. Wade, “Proton irradiation-induced metal voids in gallium nitride high electron mobility transistors,” Master’s thesis, Monterey, California: Naval Postgraduate School, 2015.
- [11] A. M. Wessel, “Imaging gallium nitride high electron mobility transistors to identify point defects,” Master’s thesis, Monterey, California: Naval Postgraduate School, 2014.
- [12] M. A. Iobst, “Gamma and neutron irradiation effects on biased gallium nitride transistors,” Master’s thesis, Monterey, California: Naval Postgraduate School, 2015.
- [13] Wikipedia, “Gallium nitride — wikipedia, the free encyclopedia,” 2016, online; accessed 28-Oct-2016. [Online]. Available: https://en.wikipedia.org/w/index.php?title=Gallium_nitride&oldid=768758318
- [14] M. Suzuki, T. Uenoyama, and A. Yanase, “First-principles calculations of effective-mass parameters of aln and gan,” *Physical Review B*, vol. 52, no. 11, p. 8132, 1995.
- [15] U. Mishra and J. Singh, *Semiconductor device physics and design*. Springer Science & Business Media, 2007.
- [16] S. M. Sze and K. K. Ng, *Physics of semiconductor devices*. John Wiley & Sons, 2006.
- [17] M. Nastasi, J. Mayer, and J. K. Hirvonen, *Ion-solid interactions: fundamentals and applications*. Cambridge University Press, 1996.
- [18] F. Auret, S. Goodman, F. Koschnick, J.-M. Spaeth, B. Beaumont, and P. Gibart, “Proton bombardment-induced electron traps in epitaxially grown n-gan,” *Applied physics letters*, vol. 74, no. 3, pp. 407–409, 1999.
- [19] H. Von Bardeleben, J. Cantin, U. Gerstmann, A. Scholle, S. Greulich-Weber, E. Rauls, M. Landmann, W. Schmidt, A. Gentils, and J. Botsoa, “Identification of the nitrogen split interstitial (n- n) n in gan,” *Physical Review Letters*, vol. 109, no. 20, pp. 206–402, 2012.

- [20] S. J. Pearton, R. Deist, F. Ren, L. Liu, A. Y. Polyakov, and J. Kim, "Review of radiation damage in gan-based materials and devices," *Journal of Vacuum Science & Technology A*, vol. 31, no. 5, p. 050801, 2013.
- [21] K. Lorenz, M. Peres, N. Franco, J. Marques, S. Miranda, S. Magalhães, T. Monteiro, W. Wesch, E. Alves, and E. Wendler, "Radiation damage formation and annealing in gan and zno," in *International Society for Optics and Photonics Optoelectronics*, pp. 79 400–79 400.
- [22] S. Limpijumnong and C. G. Van de Walle, "Diffusivity of native defects in gan," *Physical Review B*, vol. 69, no. 3, p. 035207, 2004.
- [23] A. D. Koehler, T. J. Anderson, J. K. Hite, B. D. Weaver, M. J. Tadjer, M. A. Mastro, J. D. Greenlee, P. Specht, M. Porter, and T. R. Weatherford, "Degradation mechanisms of algan/gan hemts on sapphire, si, and sic substrates under proton irradiation," in *IEEE Workshop on Wide Bandgap Power Devices and Applications*. IEEE, 2014, pp. 33–35.
- [24] J. Albrecht, R. Wang, P. Ruden, M. Farahmand, and K. Brennan, "Electron transport characteristics of gan for high temperature device modeling," *Journal of Applied Physics*, vol. 83, no. 9, pp. 4777–4781, 1998.
- [25] S. Lisesivdin, A. Yildiz, N. Balkan, M. Kasap, S. Ozelik, and E. Ozbay, "Scattering analysis of two-dimensional electrons in algan/gan with bulk related parameters extracted by simple parallel conduction extraction method," *Journal of Applied Physics*, vol. 108, no. 1, p. 013712, 2010.
- [26] A. D. Koehler, T. J. Anderson, B. D. Weaver, M. J. Tadjer, K. D. Hobart, and F. J. Kub, "Degradation of dynamic on-resistance of algan/gan hemts under proton irradiation," in *IEEE Workshop on Wide Bandgap Power Devices and Applications*. IEEE, 2013, pp. 112–114.
- [27] J. J. Barnes, R. J. Lomax, and G. I. Haddad, "Finite-element simulation of gaas mesfet's with lateral doping profiles and submicron gates," *IEEE transactions on electron devices*, vol. 23, no. 9, pp. 1042–1048, 1976.

- [28] S. Bajaj, O. F. Shoron, P. S. Park, S. Krishnamoorthy, F. Akyol, T.-H. Hung, S. Reza, E. M. Chumbes, J. Khurgin, and S. Rajan, "Density-dependent electron transport and precise modeling of gan high electron mobility transistors," *Applied Physics Letters*, vol. 107, no. 15, p. 153504, 2015.
- [29] Y. Lv, Z. Lin, Y. Zhang, L. Meng, C. Luan, Z. Cao, H. Chen, and Z. Wang, "Polarization coulomb field scattering in algan/aln/gan heterostructure field-effect transistors," *Applied Physics Letters*, vol. 98, no. 12, p. 123512, 2011.
- [30] L. Lv, X. Ma, J. Zhang, Z. Bi, L. Liu, H. Shan, and Y. Hao, "Proton irradiation effects on algan/aln/gan heterojunctions," *IEEE Transactions on Nuclear Science*, vol. 62, no. 1, pp. 300–305, 2015.
- [31] S. J. Pearnton, R. Deist, F. Ren, L. Liu, A. Y. Polyakov, and J. Kim, "Review of radiation damage in gan-based materials and devices," *Journal of Vacuum Science & Technology A: Vacuum, Surfaces, and Films*, vol. 31, no. 5, p. 050801, 2013.
- [32] J. D. Greenlee, P. Specht, T. J. Anderson, A. D. Koehler, B. D. Weaver, M. Luysberg, O. D. Dubon, F. J. Kub, T. R. Weatherford, and K. D. Hobart, "Degradation mechanisms of 2 mev proton irradiated algan/gan hemts," *Applied Physics Letters*, vol. 107, no. 8, p. 083504, 2015.
- [33] D. S. Atlas, "Atlas user's manual," *Silvaco International Software, Santa Clara, CA, USA*, 2015.
- [34] A. D. Koehler, P. Specht, T. J. Anderson, B. D. Weaver, J. D. Greenlee, M. J. Tadjer, M. Porter, M. Wade, O. C. Dubon, and K. D. Hobart, "Proton radiation-induced void formation in ni/au-gated algan/gan hemts," *IEEE Electron Device Letters*, vol. 35, no. 12, pp. 1194–1196, 2014.

Initial Distribution List

1. Defense Technical Information Center
Ft. Belvoir, Virginia
2. Dudley Knox Library
Naval Postgraduate School
Monterey, California